International Journal of Machine Tools & Manufacture 153 (2020) 103554

Contents lists available at ScienceDirect

International Journal of Machine Tools and Manufacture

journal homepage: http://www.elsevier.com/locate/ijmactool

Surface formation mechanism in ultraprecision diamond turning of coarse-grained polycrystalline ZnSe

Weihai Huang, Jiwang Yan *

Department of Mechanical Engineering, Faculty of Science and Technology, Keio University, 3-14-1 Hiyoshi, Kohoku-ku, Yokohama0, 223-8522, Japan

ARTICLE INFO

Keywords:
Diamond turning
Ultraprecision machining
Polycrystalline ZnSe
Surface integrity
Phase transformation
Grain boundary

ABSTRACT

Zinc selenide is an excellent infrared optical material. In this study, ultraprecision diamond turning experiments were carried out on coarse-grained polycrystalline ZnSe (*p*-ZnSe) under various conditions and the corresponding surface formation mechanisms were investigated by examining the surface topography, chip morphology, material microstructural change, and cutting forces. Two kinds of surface defects were observed (i.e. plowing-induced micron-scale cleavage craters and tearing-induced submicron-scale tearing pits). It was determined that plowing induced micron-scale cleavage craters could be suppressed by reducing undeformed chip thickness. Furthermore, it was ascertained that tearing-induced submicron-scale tearing pits could be restrained by using a cutting tool with a zero rake angle. The minimal surface roughness was dominated by grain boundary steps formed when the cutting tool crossed twin boundaries at a large angle. A model was proposed for correlating surface defects and boundary steps with crystal orientations and cutting directions. By using a large-nose diamond tool for cutting, a smooth surface of 1.5 nm Sa was obtained. In addition, a zinc blende to cinnabar phase transformation was observed in the cutting chips, and metallization of cutting chips occurred at an extremely small undeformed chip thickness (~20 nm). Moreover, it was discovered that phase transformation inside the workpiece depends on the radius of the tool nose. The findings of this study provide an important reference for ultraprecision machining of brittle polycrystalline materials.

1. Introduction

Zinc selenide (ZnSe) is a striking infrared optical material because of its high transmissibility at infrared wavelengths [1,2], hence, it is often used in windows of high power CO_2 lasers [3,4] and lenses for night vision systems of cars with autopilot, among others. ZnSe has a relatively low hardness quality [5], but it has a high brittleness quality [6], making it very difficult to be machined. The conventional method for creating optical surfaces with ZnSe is chemo-mechanical polishing [7,8]. However, the polishing efficiency thereof is low. Besides, it is also difficult to polish complex surfaces with high accuracy. As an alternative, ultraprecision diamond turning has been proposed as a promising solution for crafting complex shapes with high surface integrity [9].

While the existing research on single-crystalline materials has been extensive, those on polycrystalline materials are relatively few. In diamond turning of reaction-bonded silicon carbide [10], a super hard polycrystalline composite material, grain dislodgement became a major reason for surface roughness. In diamond turning of polycrystalline titanium [11], a low elastic modulus metal material with low thermal conductivity, it was found that the cracks could spread along the boundaries of large grains. In diamond turning of polycrystalline copper [12], a soft and ductile metal material, it was determined that surface crack patterns were less likely to occur. However, polycrystalline ZnSe, a soft and brittle material with different mechanical properties from the aforementioned polycrystalline materials, may result in a distinct difference in terms of the cutting mechanism. Zong et al. [9] studied oblique diamond turning of polycrystalline zinc sulfide (ZnS), whose mechanical property is, to some extent, similar to polycrystalline ZnSe, albeit less brittle than the latter, potentially causing different machinability, whether it be microscale or nanoscale.

For ultraprecision diamond turning of ZnSe, several studies have been conducted. Fang et al. [13] conducted diamond turning experiments on ZnSe (crystal structure unknown) and achieved nanometric surface finishes by using a zero rake angle tool. They mentioned that fractures would occur when a highly negative rake tool is used, however, they failed to clarify their reason for such. Shojaee et al. [14] investigated the effects of cutting parameters on residual stress as well as the crystal quality of a machined surface in diamond turning of

* Corresponding author.
E-mail address: yan@mech.keio.ac.jp (J. Yan).

https://doi.org/10.1016/j.ijmachtools.2020.103554
Received 1 February 2020; Received in revised form 27 March 2020; Accepted 29 March 2020
Available online 10 April 2020

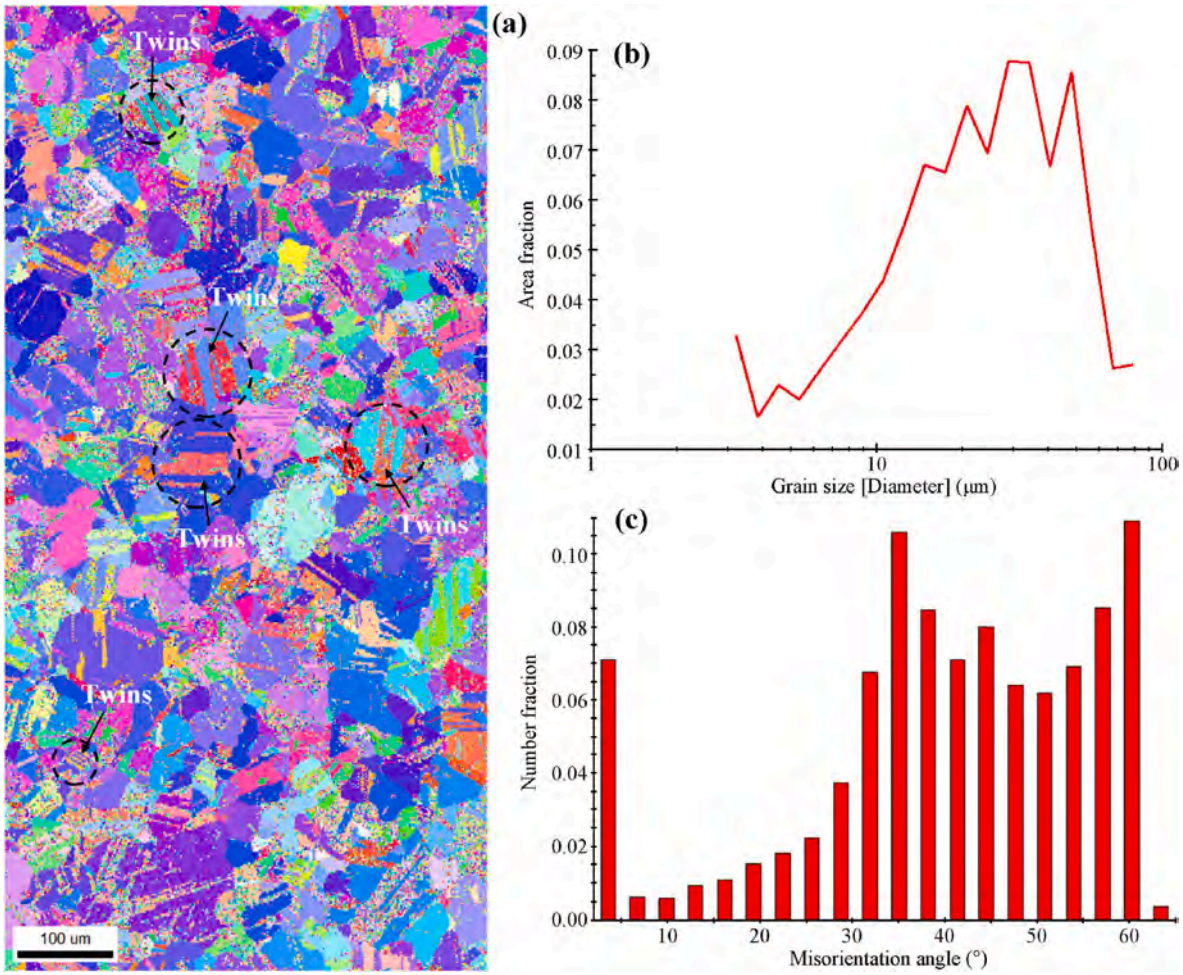

Fig. 1. (a) EBSD IPF map; (b) grain size distribution; and (c) misorientation angle distribution of *p*-ZnSe.

polycrystalline ZnSe (*p*-ZnSe). They found that certain grains or twins exhibit signs of fracture, but the relationship between the fracture and the crystallographic orientation was not characterised. Li et al. [15] investigated the ultraprecision diamond turning capability of physical vapour deposited *p*-ZnSe on a smooth surface which met the requirement for the infrared optical image systems. They found that the intended result was achieved by setting low feed rates and depths of cuts. However, even the fine finished surface still had some defects, with the formation mechanism of which kept unrevealed. Xiao et al. [16] conducted plunge-cutting experiments of *p*-ZnSe whose grain size was at the submicron level. They reported that grain dislodgement dominated the surface formation and that a larger brittle-ductile transition depth could be realised by using a tool with a highly negative rake angle or a large nose radius. It should be noted that the effect of the rake angle reported by Xiao et al. [16] is exactly contrary to that reported by Fang et al. [13]. The reason might be that the workpieces used in those studies had different crystal structures, leading to different material removal mechanisms. However, the relationship between ultraprecision machinability and workpiece crystal structure has not been well-understood. Moreover, it is inferred that the machining-induced changes of the crystal structure (i.e. phase transformation) might have significant effects on the material machinability. However, up to date, there has not been any systematic study on the phase transformation of ZnSe in diamond turning.

Currently, ZnSe windows used for infrared systems are mostly *p*-ZnSe due to its low production cost, the grain size of which being a few tens or hundreds of microns [15,17], far larger than that used in the study of Xiao et al. [16]. For coarse-grained polycrystalline materials, grain dislodgment may be suppressed, but grain boundary step (i.e. a height difference between two adjoining crystal grains appearing at their common border due to the crystallographic effect in the material property) is a critical factor of surface roughness [18,19]. Nevertheless, the relationship between the formation of grain boundary step with cutting conditions is still unclear. The grain boundary step may result from the different elastic recovery of grains following tool pass [20,21] or anisotropic plasticity dominated by dislocation slip and grain boundary accommodation, as shown by finite element simulations [22,23]. Liu et al. [24], through a molecular dynamics simulation, concluded that sub-grains with transitional crystal orientations could be formed at the grain boundary through the plowing of the cutting edge and crystal rotation. The misalignment in the slip directions between sub-grains and original grains resulted in the grain boundary step. However, these arguments have not yet been verified by experimental studies.

In this study, ultraprecision diamond turning tests were performed on coarse-grained *p*-ZnSe. The mechanisms of surface defects generation, phase transformation, and grain boundary step formation, for the tool nose radius, cutting conditions, and crystallographic orientation, were systematically investigated. The phase transformation behaviours in both the machined surface and the cutting chips were identified and compared. Finally, a smooth surface without detectable defects was realised by optimising the cutting conditions. The findings of this study provide insights into the fundamental physics of machining brittle polycrystalline material.

Table 1
Workpiece material.

Material	CVD polycrystalline ZnSe
Workpiece size	Φ 25 mm × 3 mm
Grain size	3–80 μm
Hardness	1.6 ± 0.3 GPa
Fracture toughness	0.87 ± 0.15 MPa $m^{1/2}$

2. Material and methods

2.1. Material

Chemical vapour deposited (CVD) ZnSe cylinders, 25 mm in diameter and 3 mm in thickness, were used as workpieces. According to the material manufacturer, the grain size ranged from 20 to 100 μm. The microstructure distributions of the workpieces were detected using an electron backscatter diffraction (EBSD) detector, from EDAX Inc., equipped on a field emission scanning electron microscope (FE-SEM, GeminiSEM 500, ZEISS). Fig. 1(a) shows the inverse pole figure (IPF) map of the workpieces. Many twins are observable in the microstructure of the *p*-ZnSe, as indicated by the black circles in Fig. 1(a). The corresponding grain size distribution and misorientation angle distribution were determined using TSL OIM analysis software, as shown in Fig. 1(b) and (c). From the figure presented in Fig. 1(b), the range of the grain size was estimated to be approximately 3–80 μm and the peak grain size to be around 30–50 μm. Fig. 1(c) shows that the microstructure contains a

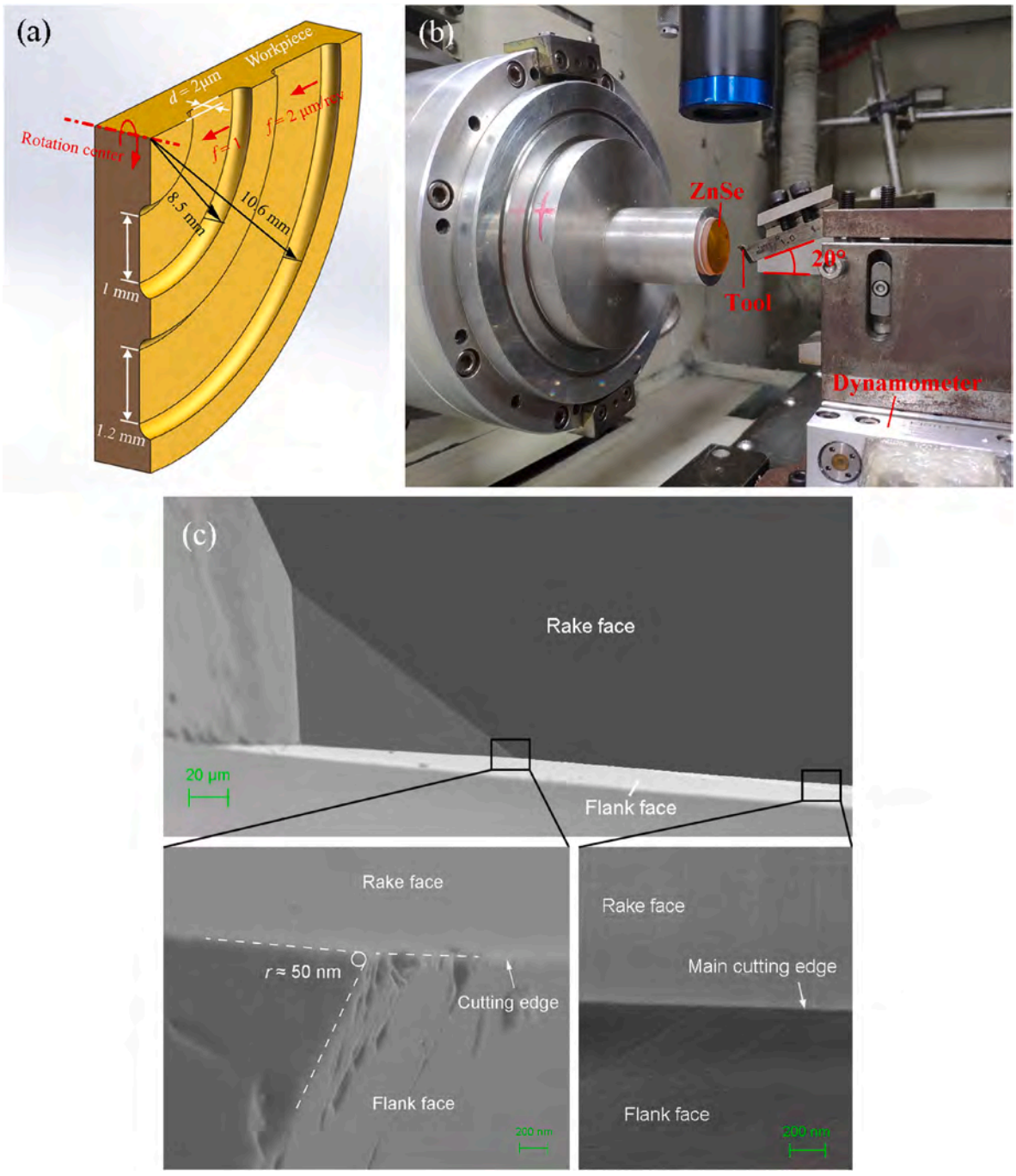

Fig. 2. (a) Schematic of workpiece dimensional for face turning by using a round-nosed tool; (b) photograph of the main section of experimental setup; (c) SEM image of the cutting edge of the *R*10 tool.

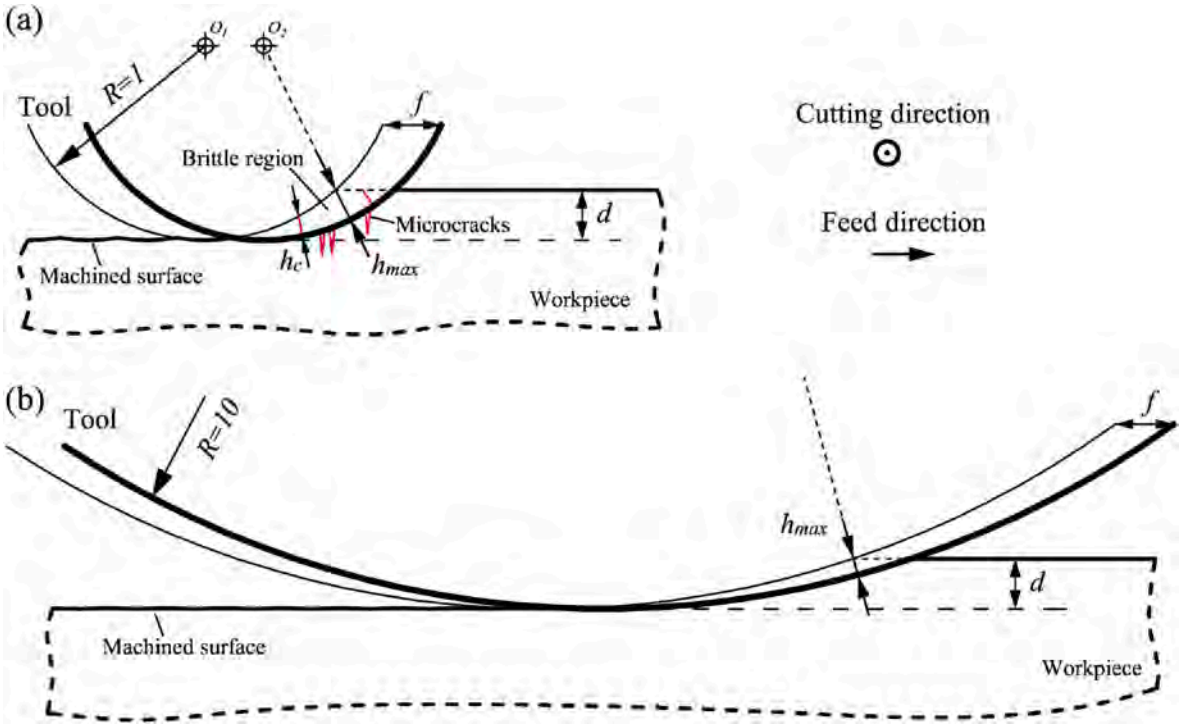

Fig. 3. Schematic of the change of undeformed chip thickness in diamond turning by using round-nosed tools with different nose radii: (a) $R = 1$ mm; (b) $R = 10$ mm.

large fraction of high-angle grain boundaries.

Nanoindentation experiments with a Berkovich and a cube-corner indenter were carried out using a nanoindentation instrument (ENT1100a, Elionix Inc.) to characterise the hardness and fracture toughness of the material, respectively. The indentations were made on selected large crystal grains rather than across grain boundaries. The hardness (H) is evaluated by the following equation [25]:

$$H = \frac{P}{A} \tag{1}$$

where P is the maximum applied load and A is the contact area of the indentation at the maximum load. For the Berkovich indenter, the area function is determined as follows [25]:

$$A = 24.675h^2 + 0.562h + 0.003216 \tag{2}$$

where h is the indentation depth.

The fracture toughness (K_{IC}) was determined according to the method presented by Zhang et al. [26]:

$$K_{IC} = \lambda \left(\frac{W_u}{W_t}\right)^{-1/2} \frac{P}{c^{3/2}} \tag{3}$$

where λ is a constant number independent of the material, which is approximately 0.0695 for a cube-corner indenter. W_u refers to the unloading work and W_t pertains to the loading work. c is the length of the radial crack trace on the material surface after the withdrawal of the indenter.

The hardness and fracture toughness measured by nanoindentation tests are 1.6 ± 0.3 GPa and 0.87 ± 0.15 MPa $m^{1/2}$, respectively. These bulk material properties are similar to those of the single-crystal ZnSe (111) [27]. The information on the workpiece is summarised in Table 1.

Table 2
Cutting conditions.

Cutting tool	Single-crystal diamond tool	
Tool nose radius	1 mm	10 mm
Rake angle α	0°, −20°	0°
Relief angle γ	8°, 28°	10°
Feed rate f	1, 2 μm/rev	0.5, 1 μm/rev
Cutting speed v	94–106 m/min	
Depth of cut d	2 μm	
Environment	Dry cutting with vacuum suction	

2.2. Experimental setup and conditions

Face turning experiments were carried out using an ultraprecision turning machine (ASP-15, NACHI-FUJIKOSHI Co., Ltd.). As shown in Fig. 2(a), two regions with widths of 1.2 and 1 mm were cut at feed rates of 2 and 1 μm/rev, respectively, with the depth of the cuts at 2 μm. The initial points of the two regions in the radial direction of the workpiece are at radii of 10.6 and 8.5 mm, respectively. To ensure that the cutting speeds are approximately the same for the two regions, the spindle rotation rates were set to 1600 and 2000 rpm, respectively. The cutting forces were measured by a three-component piezoelectric dynamometer (Kistler 9256C2) mounted below the tool holder. The photograph of the experimental setup is shown in Fig. 2(b).

First, a single-crystal diamond tool with a nose radius of 1.0 mm ($R1$), a rake angle of 0°, and a relief angle of 8° was used for experimentation. By using a tailor-made tool holder, the tool rake angle was changed from 0° to −20° (the relief angle was changed from 8° to 28°, accordingly) to investigate the effect of tool angles.

To achieve an extremely small undeformed chip thickness without reducing the machining efficiency, previous researchers have attempted to make use of a cutting tool with a large nose radius [28]. Fig. 3 shows the schematic of the undeformed chip thickness in diamond turning by using round-nosed tools with different nose radii. Provided that other parameters (i.e. depth of cut and feed rate) are the same, a larger tool nose radius leads to a thinner undeformed chip, as described by equations A3 and A4 in the Appendix. In this study, a tool with 10 mm nose radius ($R10$), a rake angle of 0°, and a relief angle of 10° was used for cutting. The results thereof were compared with those corresponding to the $R1$ tool. The edge radius of both the $R1$ and $R10$ tools was approximately 50 nm, as polished by Tokyo Diamond Tools Mfg. Co., Ltd. Fig. 2(c) shows a high-magnification image of the cutting edge of the $R10$ tool

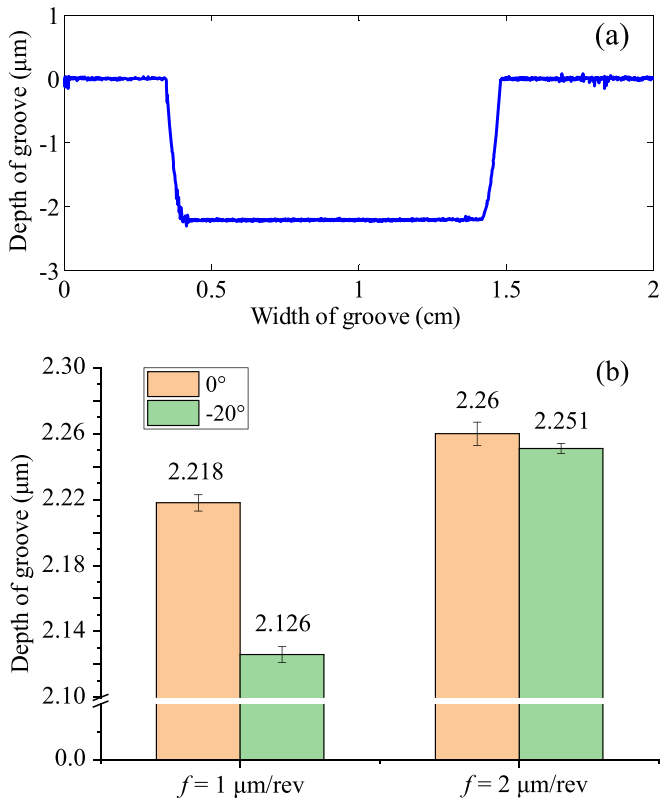

Fig. 4. (a) Cross-section profile of a groove machined under $f = 1$ μm/rev, $\alpha = 0°$; (b) depths of grooves machined under different conditions.

using FE-SEM (MERLIN Compact, ZEISS). The cutting conditions for the *R*1 and *R*10 tools are summarised in Table 2. At a feed rate of 1 μm/rev and depth of cut of 2 μm, the maximum undeformed chip thickness (h_{max}) for the *R*1 tool was 63 nm. The same was reduced to 20 nm for the *R*10 tool. The experiment was performed under a dry cutting environment, without using a coolant, in order to collect cutting chips for SEM observation. Dry cutting is likewise helpful in the actual manufacturing process of ZnSe components. Given that ZnSe material is toxic, dry cutting chips are relatively easy to be collected by vacuum suction while wet chips are extremely difficult in terms of collection and proposal.

2.3. Measurement and characterisation methods

The cross-sectional profiles of the machined regions were measured by a laser-probe 3D surface profilometer (NH-3SPs, Mitaka Kohki Co., Ltd.). Thereafter, a laser micro-Raman spectrometer (NRS-3100, JASCO) was used to detect the structural change in the material after machining. The machined surface, collected chips, and tool wear were observed using FE-SEM (MERLIN Compact, ZEISS). The crystallographic orientation texture of the machined surface was examined using EBSD. The 3D topography of the machined surface was measured using a white light interferometer (Talysurf CCI 1000, Taylor Hobson).

3. Results for small nose radius (*R*1) tool

3.1. Surface topography

Four regions were machined under four different conditions: (i) $f = 1$ μm/rev, $\alpha = 0°$; (ii) $f = 2$ μm/rev, $\alpha = 0°$; (iii) $f = 1$ μm/rev, $\alpha = -20°$; (iv) $f = 2$ μm/rev, $\alpha = -20°$. A typical cross-section profile of a groove machined under condition (i) is shown in Fig. 4(a). Fig. 4(b) shows the depth of each groove. It can be noted in Fig. 4(b) that the depths of all grooves are deeper than the set depth of cut, possibly because of the tool-

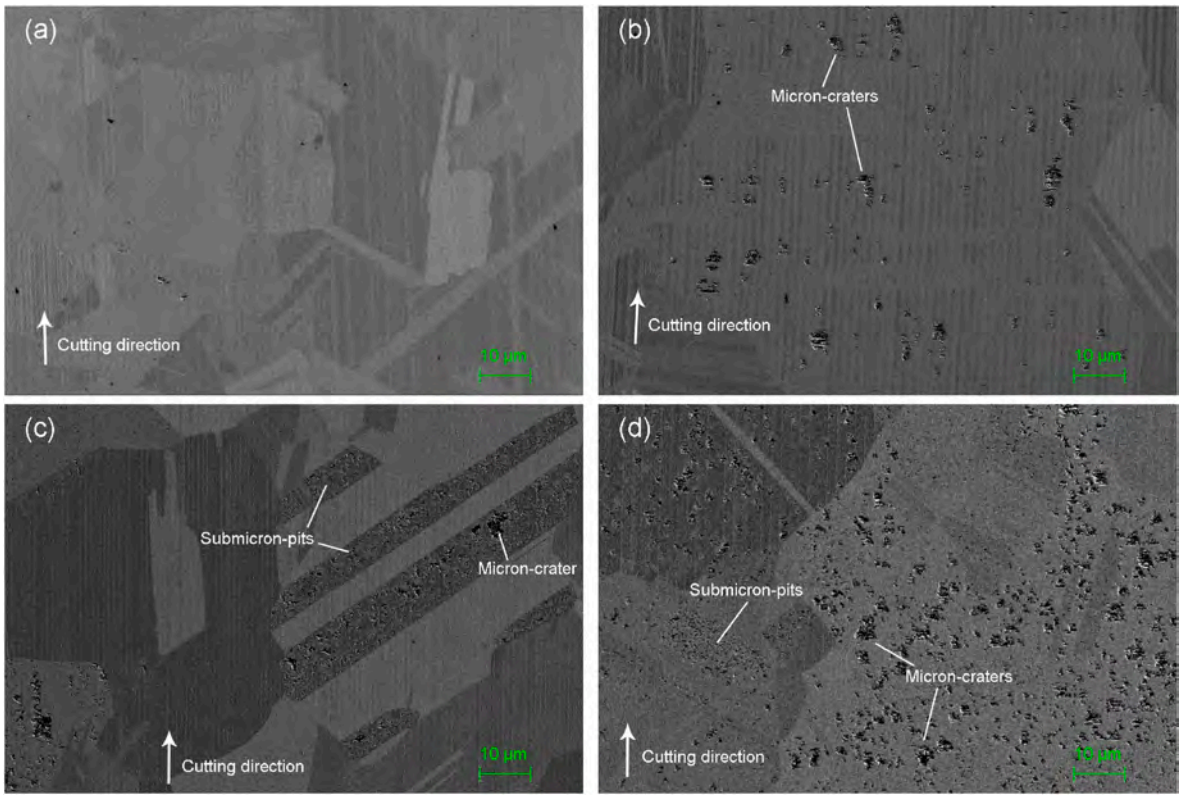

Fig. 5. SEM images of groove surfaces machined under conditions: (a) $f = 1$ μm/rev, $\alpha = 0°$; (b) $f = 2$ μm/rev, $\alpha = 0°$; (c) $f = 1$ μm/rev, $\alpha = -20°$; and (d) $f = 2$ μm/rev, $\alpha = -20°$.

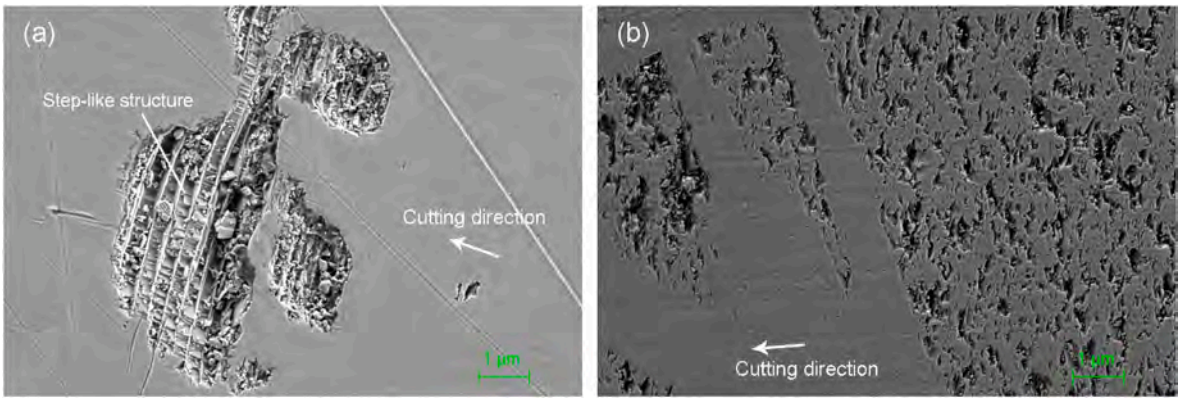

Fig. 6. Close-up views of (a) micron-craters on the surface machined at $f = 2$ μm/rev, $\alpha = 0°$ and (b) submicron-pits on the surface machined at $f = 2$ μm/rev, $\alpha = -20°$.

workpiece alignment error. Since it is an insignificant systematic error and it does not affect the comparison of the relative differences among the grooves, we neglected the impact of this error. The difference in the depths of the grooves is supposed to be caused by the different degrees of elastic recovery of the material under different cutting conditions. Given the same feed rate, the elastic recovery of the machined surface was determined to be larger under a negative rake angle, possibly since a more significant plowing effect relating to the large negative rake angle tool increases the minimum undeformed chip thickness [29]. This issue will be subsequently discussed in Section 3.4. Considering the same rake angle, the elastic recovery of the machined surface was ascertained to be larger at a smaller feed rate, possibly because a brittle fracture could occur during material removal with a large feed rate, leading to a weakened plowing effect and resulting in lesser elastic recovery. With a low feed rate, the undeformed chip thickness is lessened. As a result, ductile removal could occur more frequently during machining, resulting in higher elastic recovery.

Fig. 5 shows SEM images of the groove surfaces machined under four different conditions. The crystal grains of varied orientations can be differentiated from each other by showing different gray levels. Fig. 5(a) shows a smooth surface machined under $f = 1$ μm/rev, $\alpha = 0°$, which has few defects. Increasing the feed rate to 2 μm/rev, it can be observed that micron-craters appear on some grains as shown in Fig. 5(b). However, when the tool rake angle was changed to $-20°$, surface defects were observed under both feed rates (i.e. at 1 μm/rev, the surface defects on the grains were dominated by submicron-pits, as shown in Fig. 5(c); and at 2 μm/rev, the surface defects on the grains were composed of micron-craters and submicron-pits, as shown in Fig. 5(d)). Noteworthy is the fact that in Fig. 5(c), the defects formed at the small twin grains. Moreover, it is likewise important to note that in Fig. 5(d), the defects formed at the large grains. The formation of defects in the grains seems to be independent of the grain size, which is inconsistent with the results of turning polycrystalline metal (i.e. the crack formation is related to the grain/twin size due to different levels of stress concentration on unit per unit volume of grain boundary) [11]. This might be because the machining scale is far smaller than the grain/twin size in ultraprecision cutting of ZnSe, such that the effect of crystal orientation is stronger than that of grain size. If fine-grain or nano-crystal ZnSe is used as the workpiece, however, the result might be different [16].

The detailed observation of micron-crater and submicron-pits are shown in Fig. 6(a) and (b), respectively. In the observation regarding the micron-crater, a step-like structure that is perpendicular to the cutting direction can be seen. It is assumed that this step-like structure is caused by the crack propagation along two different cleavage planes that cross each other. The cleavage plane of ZnSe is {110} [30,31], hence the two cleavage planes form 90°, which is in line with the feature of step-like structures. A schematic diagram of the simplest situation of the relative spatial relation between cutting direction and cleavage planes for cleavage fracture formation is shown in Fig. 7. In contrast, for the observation on the submicron-pits, the pit size along the cutting direction is perceived to be smaller in size than that which is vertical to the cutting direction. This may be caused by the tearing and spalling of the material after the tool has passed through it. This issue will be discussed in Section 3.5.

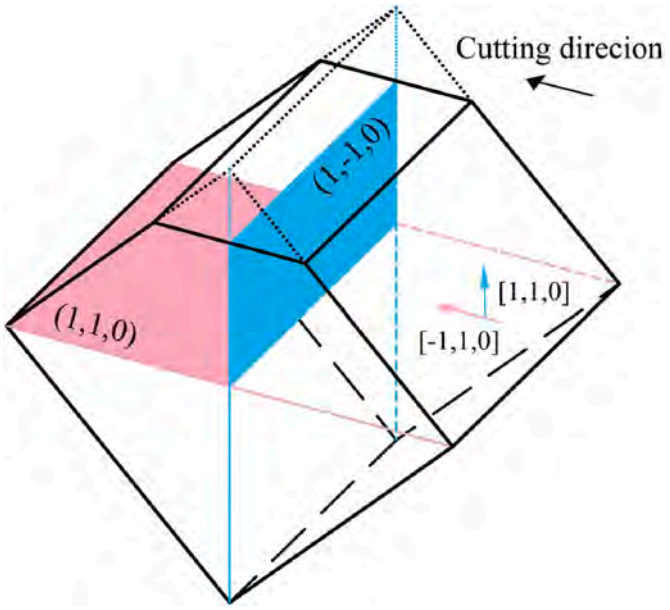

Fig. 7. A schematic diagram of the simplest situation of relative spatial relation between cutting direction and cleavage planes for cleavage fracture formation.

For each SEM image shown in Fig. 5, the distribution of defect size has been analysed using the ImageJ software. Based on the characterisation of the surface defect pattern in Fig. 6, the defect area whose size was found to be in the range of 0.5–20 μm^2 was measured. The histogram was thereafter plotted, as shown in Fig. 8. It can be observed from the histogram that the number of large-size defects under conditions (b) and (d) are more than that under conditions (a) and (c). This is caused by the higher undeformed chip thickness h in conditions (b) and (d). However, under the same h, the number of small-size defects formed at a rake angle of $-20°$ (conditions (c) and (d)) are more than those at a rake angle of 0° (conditions (a) and (b)). Thus, it can be concluded that the micron-craters tend to form at a higher feed rate (2 μm/rev), while the submicron-pits tend to form at a negative ($-20°$) rake angle.

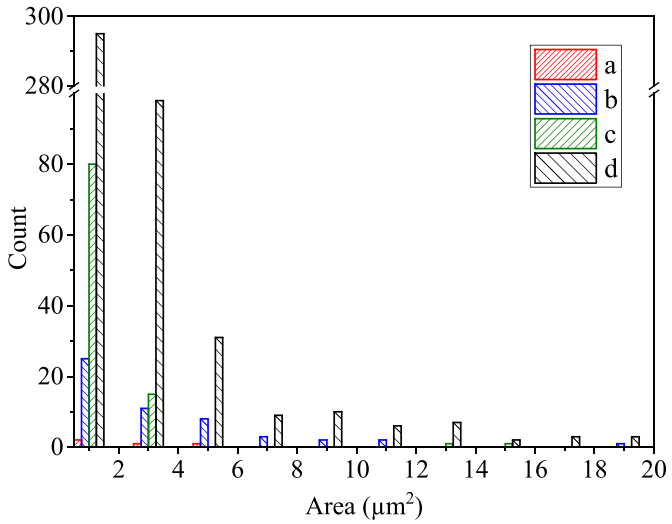

Fig. 8. Distribution of defect size under conditions: (a) $f = 1$ μm/rev, $\alpha = 0°$; (b) $f = 2$ μm/rev, $\alpha = 0°$; (c) $f = 1$ μm/rev, $\alpha = -20°$ and (d) $f = 2$ μm/rev, $\alpha = -20°$.

3.2. Cutting chips morphology

Continuous or partially segmented chips were found in each cutting condition, as shown in Fig. 9. By using a 0° rake angle tool at a feed rate of 1 μm/rev, chips of needle were dominant shaped, as shown in Fig. 9 (a). As the feed rate was increased to 2 μm/rev, flake-shaped chips emerged, as shown in Fig. 9(b). However, by using a −20° rake angle tool, flake-shaped chips were observed at both feed rates of 1 and 2 μm/rev, as shown in Fig. 9(c) and (d), respectively.

The close-up views of needle-shaped and flake-shaped chips are shown in Fig. 10(a) and (b), respectively. It can be seen in Fig. 10(a) that the needles are actually very small curls. For both types of chips, lamellar structures with a constant spacing of tens of nanometres can be observed on one side of the chips. This indicates that the chip results from a periodic shear deformation in the primary shear zone [32]. It can also be seen that the thickness of the needle-shaped chip (Fig. 10(a)) is much smaller than that of the flake-shaped chip (Fig. 10(b)).

Fig. 11 shows the chips having irregular particle shapes formed by brittle fracture. When the rake angle is at −20°, chip morphologies of $f = 1$ and 2 μm/rev were observed, as shown in Fig. 11(a) and (b), respectively. It can be seen that very small chips, whose average size is less than 300 nm, were generated. The size of such chips is smaller than that of submicron-pits on the machined surface, as shown in Fig. 6(b). This suggests that such chips might be peeled off or pulled out from the machined surface. On the other hand, when $f = 2$ μm/rev, the chip morphologies at $\alpha = 0°$ and −20° can be observed, as shown in Fig. 11(c) and (d), respectively. The blocky chips with a size of over 600 nm that were generated are observed to be much larger than the submicron-pits. Such an appearance of chips is similar to that of chips formed by crack propagation and brittle fracture [33], indicating that the material is removed in a brittle mode.

3.3. Raman spectroscopy

To investigate the possible phase transformation of the workpiece material caused by cutting, micro-Raman spectroscopy analysis was conducted. Fig. 12 shows the Raman spectra of the non-machined surface, the machined surface at $f = 1$ μm/rev, $\alpha = 0°$, and the cutting chips at $f = 1$ μm/rev, $\alpha = 0°$ and −20°. The Raman spectra of the non-machined surface and machined surface show three peaks at around 142.8, 205.8, and 252.4 cm^{-1} that correspond to the transversal acoustic (2 TA) phonon mode, the transversal optical (TO), and the longitudinal optical (LO) phonon modes of ZnSe, respectively [34]. From this result, no phase transformation was detected on the machined surface. In the Raman spectrum of the cutting chips, however, the 2 TA phonon peak disappeared in both cases while the TO splitting mode was observed at 205.9 and 207.1 cm^{-1}. At the same time, the TO phonon peak shifted to 250.9 and 249.6 cm^{-1} and the LO phonon peak shifted to 270.9 and 266.1 cm^{-1}. This type of Raman spectra are in agreement with the Raman spectrum of ZnSe under high pressure [35]. The appearance of

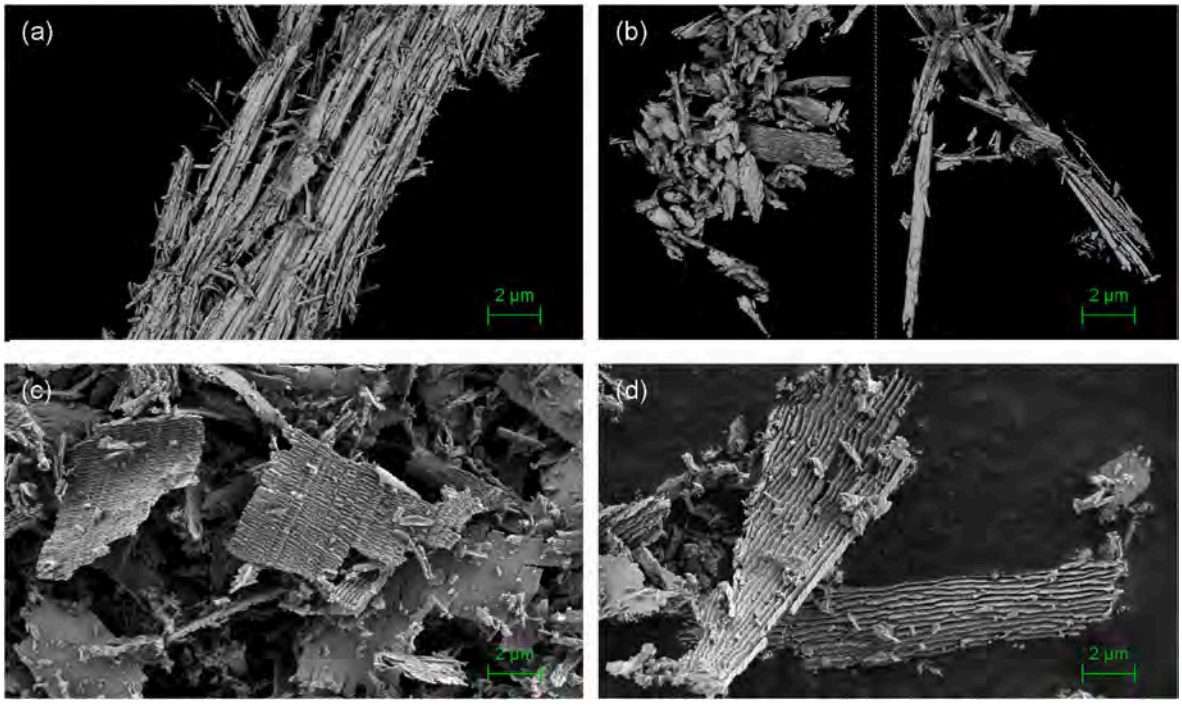

Fig. 9. SEM images of cutting chips formed under conditions: (a) $f = 1$ μm/rev, $\alpha = 0°$; (b) $f = 2$ μm/rev, $\alpha = 0°$; (c) $f = 1$ μm/rev, $\alpha = -20°$ and (d) $f = 2$ μm/rev, $\alpha = -20°$.

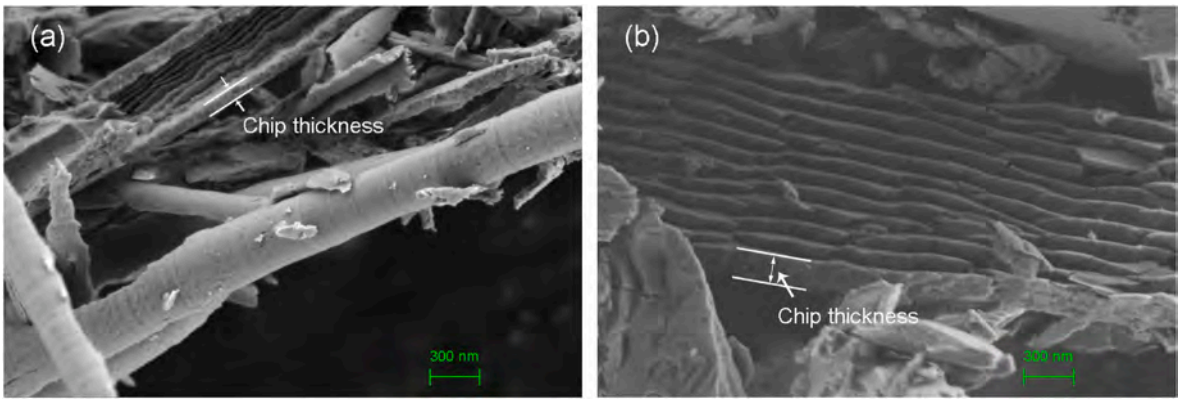

Fig. 10. Close-up views of (a) needle-shaped chip; (b) flake-shaped chip.

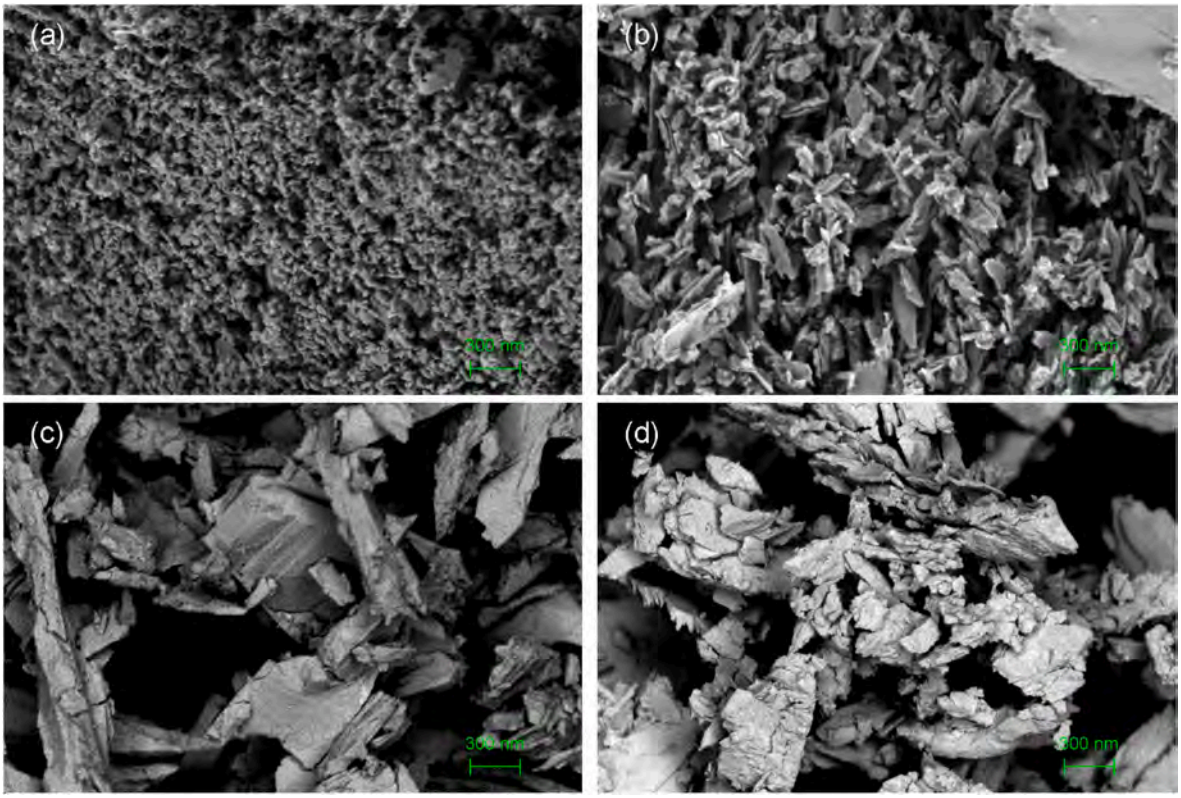

Fig. 11. Close-up views of particle-shaped chips which was observed at (a) (a) $f = 1$ μm/rev, $\alpha = -20°$; (b) $f = 2$ μm/rev, $\alpha = -20°$; (c) $f = 2$ μm/rev, $\alpha = 0°$ and (d) $f = 2$ μm/rev, $\alpha = -20°$.

the TO splitting mode indicates that ZnSe is transformed from zinc blende to a cinnabar structure when subjected to a pressure level higher than 5.5 GPa [35]. The shifts of the TO and LO phonon peaks at $\alpha = 0°$ are more than those at $\alpha = -20°$, indicating that the cutting pressure is higher at $\alpha = 0°$. In general, the two Raman spectra of cutting chips show that the cutting chips undergo a phase transformation.

It is worth mentioning that in the diamond turning of silicon, both cutting chips and machined surfaces are associated with similar phase transformation paths [36] induced by the high hydrostatic pressure [37]. However, in the diamond turning of ZnSe, phase transformation could not be detected from the machined surface. This may be attributed to the fact that the stress in the material below the tool can be resolved into the hydrostatic stress induced by the tool compression as well as the deviatoric stress induced by tool friction. Although the hydrostatic stress is predominant, thereby causing phase transformations, the phase transformation is reversed right after decompression [38] or the transformed layer is too thin to be detected by laser Raman measurement [39]. This is because the deviatoric stress, in this case, is too weak to maintain the pressure-induced phase transformation. In the cutting chips, however, the shear stress was sufficiently strong which could uphold the maintenance of the pressure-induced phase transformation even after chip removal.

3.4. Cutting force

The principal and thrust forces were measured during machining. A typical real-time curve of cutting force under $f = 2$ μm/rev, $\alpha = 0°$ is shown in Fig. 13(a). A significant fluctuation was observed when the tool was inserted into the surface. Thereafter, the cutting force became stable when the tool started feeding along the radial direction of the

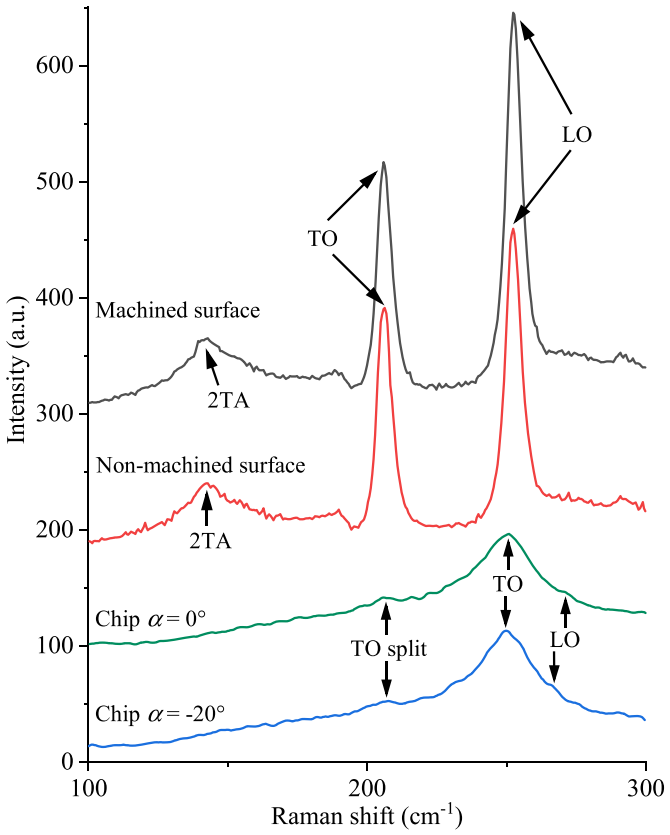

Fig. 12. Raman spectra of non-machined surface and machined surface as well as cutting chips.

workpiece. The cutting force under this cutting condition was determined by calculating the mean of the cutting force (from 17 s to 35 s). Fig. 13(b) presents a comparison of the forces among four different conditions. It can be seen that both the principal and thrust forces at the 0° rake angle (8° relief angle) are larger than those at the −20° rake angle (28° relief angle). Since a large portion of thrust force is contributed by the spring back of machined surface acting on the tool [40], the reduction of thrust force at the −20° rake angle might be due to the decreased flank face/workpiece contact area. It is worth noting that the principal force was likewise decreased when a negative rake angle was used, showing an opposite trend compared with cutting other materials (i.e. carbon steel and single-crystal silicon) [41,42].

In cutting steel, a typical ductile material, the phenomenon wherein the principal force increases by using a negative rake angle tool may be attributed to the increased tool/chip contact area [41]. Since the undeformed chip thickness h is in micron-scale for cutting steel, the tool/chip contact area could be the predominant factor in determining principal force. In cutting silicon, a typical hard brittle material, h is in the submicron scale. However, the hardness of silicon is at a very high level, thus the contact pressure between the tool and workpiece could reach a very high level when a negative rake angle tool is used, causing the structure of silicon to change from its original diamond cubic to a metallic state [42]. Hence, the shear deformation of the metallic phase dominates the general mechanism of material removal, leading to a larger principal force.

In cutting ZnSe, a typical soft-brittle material, h is in the submicron scale, which is similar to that in terms of cutting silicon. Although the phase transformation occurs during the cutting process, the contact pressure is not high enough to cause the metallization of material, even when a negative rake angle tool is used (Fig. 12) due to the low level of hardness of ZnSe. This indicates that the negative rake angle tool is unable to facilitate the ductile removal of ZnSe. On the other hand, another factor should be noted, especially in terms of submicron-scale cutting, that is, the minimum undeformed chip thickness h_{min}, below which no material removal will occur [43–45]. The h_{min} could greatly affect the cutting force in submicron-scale cutting, considering that the ratio of h_{min} to h is relatively high. Several studies have reported that the h_{min} increases with the tool edge radius, leading to increased plastic flow of material downwards the cutting tool and a decreased shear deformation of material in front of the tool rake face [46–48]. Besides, as the rake angle becomes a negative one, the tool becomes blunt and the equivalent tool edge radius becomes larger. Therefore, in the diamond turning of ZnSe, the reduction of the principal force at the −20° rake angle tool maybe due to the reduction of shear deformation of material in front of the tool rake face caused by the increased h_{min}. This is in line with the result, as shown in Fig. 4(b), that the depth of grooves at the −20° rake angle tool is smaller than that at the 0° rake angle tool (i.e. the material removal at the −20° rake angle tool is less than that at the 0° rake angle tool). A similar trend of force change has likewise been reported in ultraprecision turning of CaF_2, whose mechanical properties are similar to ZnSe [49].

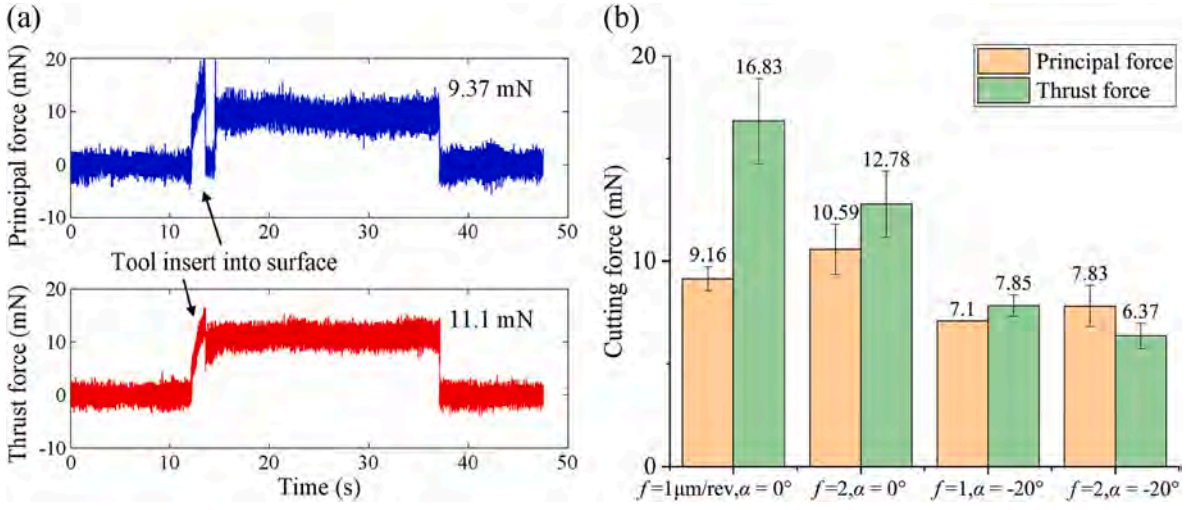

Fig. 13. (a) The real-time curve of the principle and thrust force under the condition of f = 2 μm/rev, α = 0°; (b) Comparison of cutting forces under different conditions.

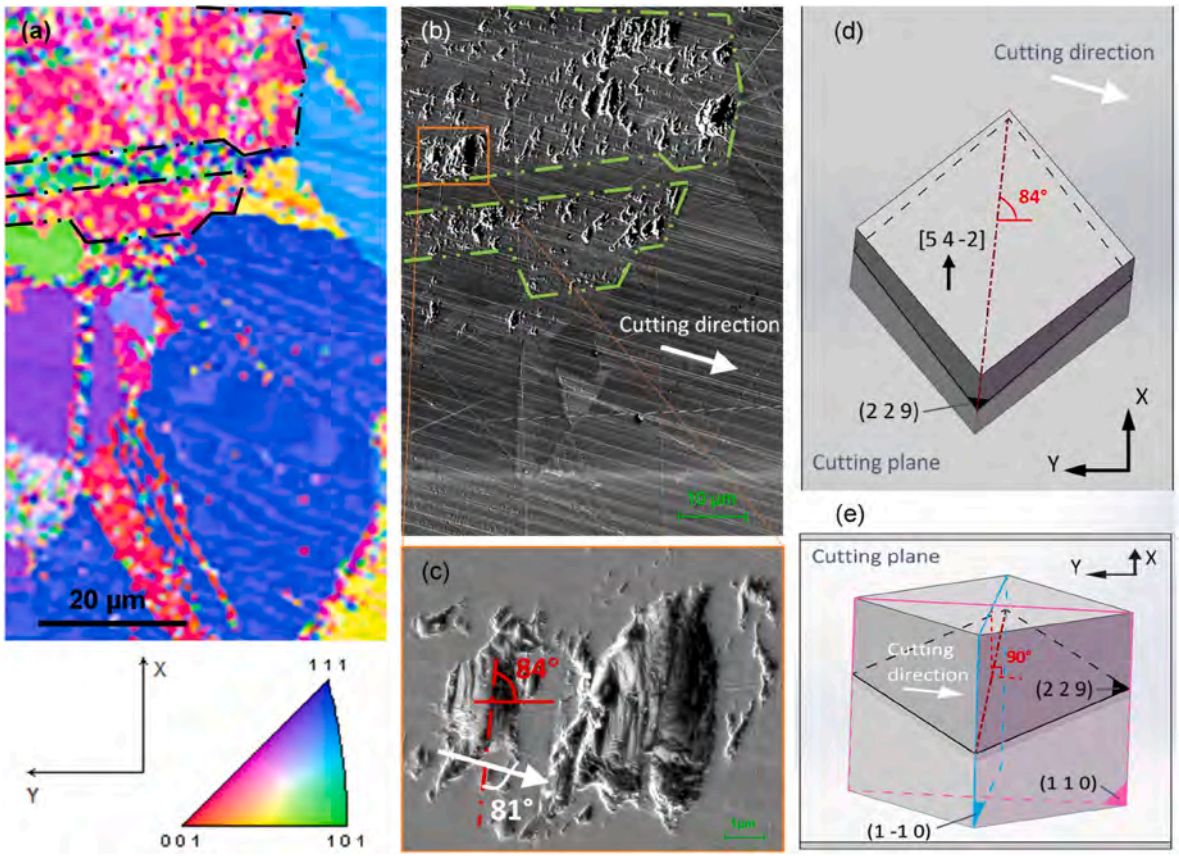

Fig. 14. (a) IPF map of a machined surface with micron-craters; (b) SEM image of the same surface in (a); (c) close-up view of a micron-crater; (d) and (e) are schematic drawings of top and oblique views of the crystal orientation of the damaged grain that is highlighted in (a) and (b) by black and green dash-dotted lines, respectively. (For interpretation of the references to colour in this figure legend, the reader is referred to the Web version of this article.)

3.5. *Crystallographic effect on surface defect formation*

As mentioned in Section 3.1, the micron-craters tend to be formed at a feed rate of 2 μm/rev while the submicron-pits tend to be formed at a −20° tool rake angle. In order to clarify the mechanism of surface defect formation, EBSD analysis of the surfaces was conducted, as shown in Figs. 14 and 15.

Fig. 14(a) illustrates the IPF map of a machined surface with micron-craters. The corresponding SEM image of the machined surface is shown in Fig. 14(b) and the close-up view of a micron-crater is shown in Fig. 14 (c). The damaged grain is highlighted by black and green dash-dotted lines in Fig. 14(a) and (b), respectively. Result shows that the damaged grain's crystal orientation, represented by Miller indices, is (2 2 9) [5 4 –2]. Consequently, the spatial relationship between the damaged grain and cutting plane can be illustrated, as shown in Fig. 14 (d) and (e), respectively. Given that the cleavage plane of ZnSe is {1 1 0}, the line formed by the intersection of the cleavage plane (1 -1 0) and the cutting plane makes an angle of 84° with the *y*-axis. It is further observed that the cleavage plane sits at an angle of 90° with the cutting plane. In the close-up view of a micron-crater (Fig. 14(c)), the step-like structure and *y*-axis meet at the angle of 84°, which is same as the angle between the *y*-axis and the line of intersection of cleavage/cutting planes (Fig. 14 (d)), thereby indicating that the crack was propagated along the cleavage plane. Moreover, the step-like structure makes an angle of 81° with the cutting direction, which is consistent with the finding that the cutting direction is almost perpendicular to the cleavage plane (Fig. 14(e)). As a result, it can be inferred that as the cutting tool moves forward, cracks occur along the cleavage plane, which is perpendicular to the cutting plane (Fig. 14(e)). Meanwhile, cracks could also manifest along another cleavage plane (1 1 0), which is perpendicular to the cleavage plane (1 -1 0). The above brittle fracture process causes micron-craters on the machined surface, as illustrated in Fig. 16(a). Therefore, it can be argued that the grain under the condition that the cleavage plane is perpendicular to both the cutting plane and cutting direction has the lowest critical undeformed chip thickness h_c. To avoid micron-craters, the undeformed chip thickness h should be smaller than h_c throughout the whole cutting process, thereby acting as a barrier to improve the processing efficiency for a polycrystalline material.

Fig. 15(a) illustrates the IPF map of a machined surface with submicron-pits. The corresponding SEM image of the machined surface is shown in Fig. 15(b) and the close-up view of the submicron-pits is presented in Fig. 15(c). The damaged grain is highlighted by black and green dash-dotted lines in Fig. 15(a) and (b), respectively. The results show that the crystal orientation represented by Miller indices is (2 1 3) [5 2 –4]. Consequently, the spatial relationship between the damaged grain and cutting plane can be illustrated, as shown in Fig. 15(d) and (e). The line formed by the intersection of cleavage plane (1 -1 0) and cutting plane makes an angle of 78° with the *y*-axis. Furthermore, the cleavage plane sits at an angle of 79° in relation to the cutting plane (i.e. the cleavage plane is almost perpendicular to the cutting plane). In the close-up view of the submicron-pits (Fig. 15(c)), the rows of submicron-pits and *y*-axis meet at the angle of 78°, which is same as the angle between the *y*-axis and the line of intersection of the cleavage/cutting planes (Fig. 15(d)). This indicates that the crack formed along the cleavage plane. Although the angle between the row of submicron-pits and cutting direction is 83°, the cutting direction is not perpendicular to the cleavage plane because the cutting plane is not perpendicular to the cleavage plane (Fig. 15(e)). On the one hand, this implies that it is relatively difficult for the brittle fracture of such grain to manifest compared to the grain whose cleavage plane is perpendicular to both the

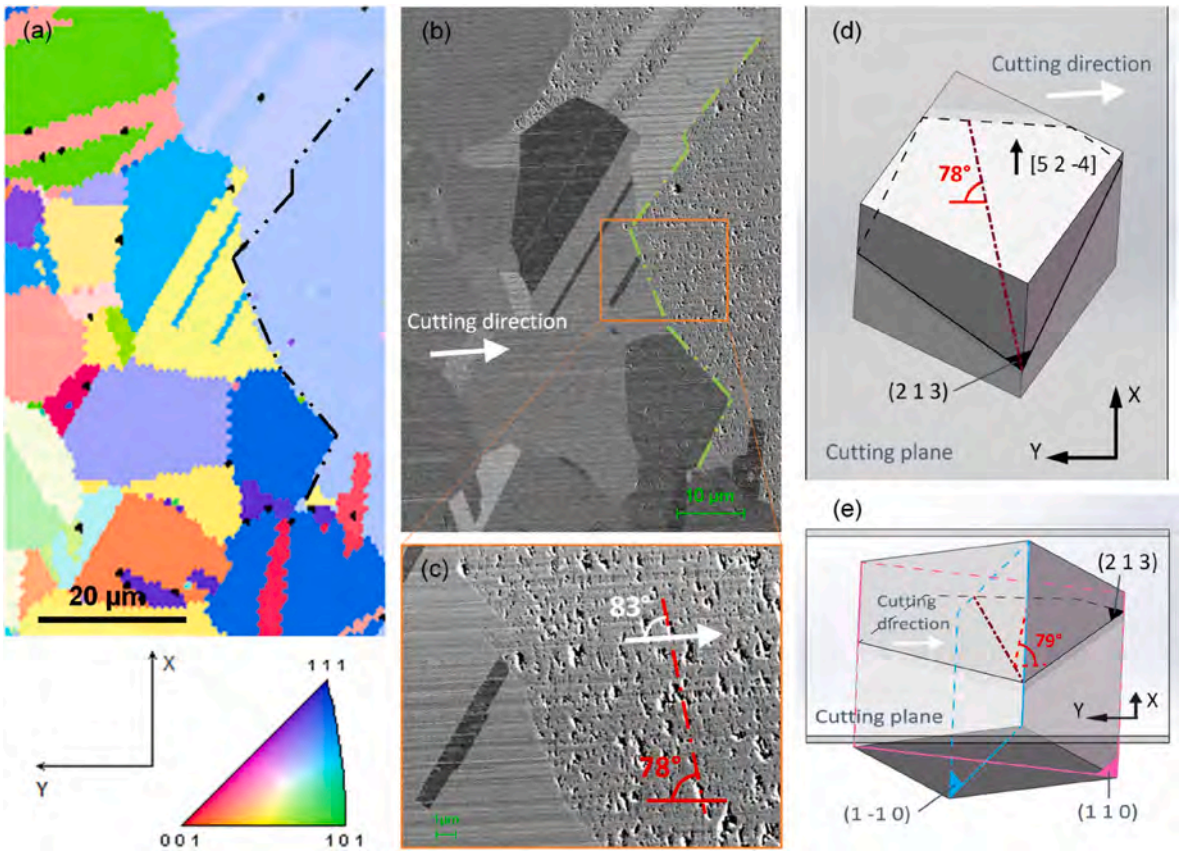

Fig. 15. (a) IPF map of a machined surface with submicron-pits; (b) SEM image of the same surface in (a); (c) close-up view of submicron-pits; (d) and (e) are schematic drawings of top and oblique views of the crystal orientation of the damaged grain that is highlighted in (a) and (b) by black and green dash-dotted lines, respectively. (For interpretation of the references to colour in this figure legend, the reader is referred to the Web version of this article.)

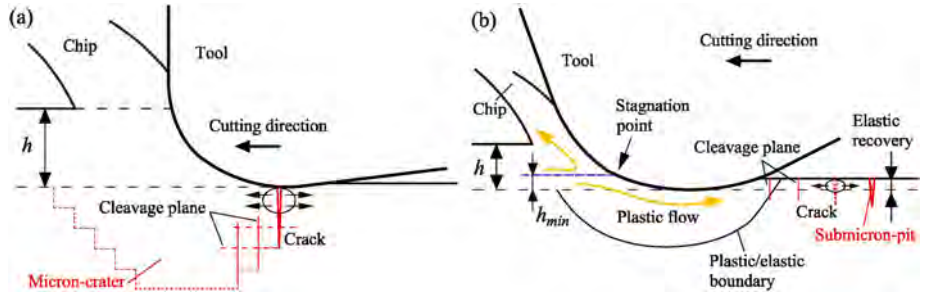

Fig. 16. Schematic model for surface defect formation: (a) micron-crater due to plowing effect, (b) submicron-pits due to tearing and spalling.

cutting plane and cutting direction. On the other hand, such submicron-pits appear when the $-20°$ rake angle tool ($\gamma = 28°$) is used, even at a feed rate of 1 μm/rev. In other words, the submicron-pits manifest at low levels of undeformed chip thickness when using the tool with a negative rake angle and a large relief angle. This means that the submicron-pits may not be caused by the plowing effect of the tool. Rather, these are caused by the peeling of the material from the machined surface after such tool passes, as shown in Fig. 16(b). When the material is found below the segment point, chip formation does not occur. Instead, the material undergoes elastic and plastic deformation and flows downward, causing a plastic/elastic deformation layer beneath the tool. Thereafter, the layer springs back after the tool passes [50,51]. Cracks caused by the elastic recovery would start forming at the machined surface along the cleavage plane that is vertical to the cutting plane, resulting in surface defect of submicron-pits.

In summary, the micron-craters are observed to cleavage microfractures, which are easily formed on the grain whose cleavage plane is perpendicular to the cutting plane and cutting direction and when the undeformed chip thickness is relatively high. This is caused by plowing effects along the cleavage planes, similar to those that occur in the cutting process of other brittle crystals such as silicon [52,53]. Moreover, it was determined that the submicron-pits were easily formed on the grain whose cleavage plane is perpendicular to the cutting plane and when a tool with a large relief angle is used. This is caused by the tearing effects along the cleavage planes during the elastic recovery of the workpiece material. The formation of submicron-pits is a special phenomenon for soft brittle materials but the same has never been reported for hard brittle materials. In addition, since ZnSe has a face-centred cubic structure, it has six {110} cleavage planes. Therefore, defects could form on many grains with different crystal orientations, as long as at least one of the aforementioned conditions is met.

According to previous studies, cracks could nucleate at the

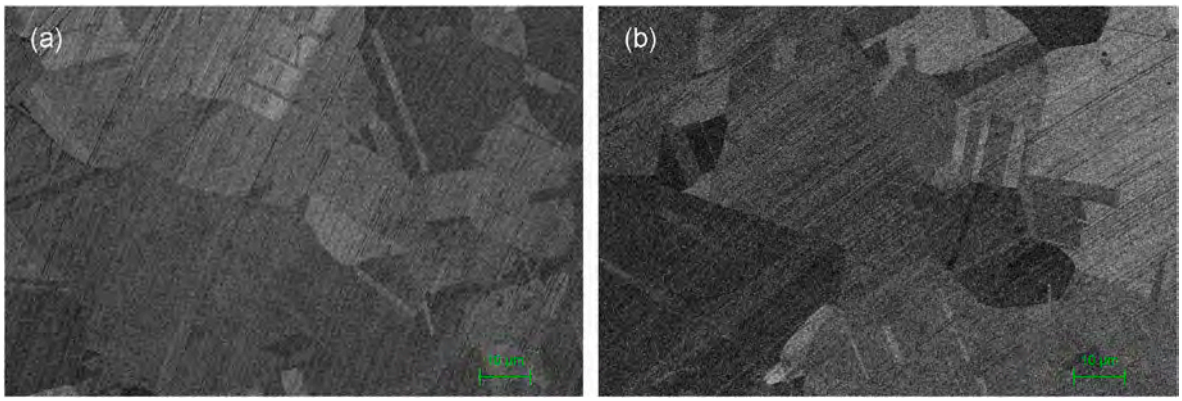

Fig. 17. SEM images randomly taken from a surface machined by using a *R*10 tool.

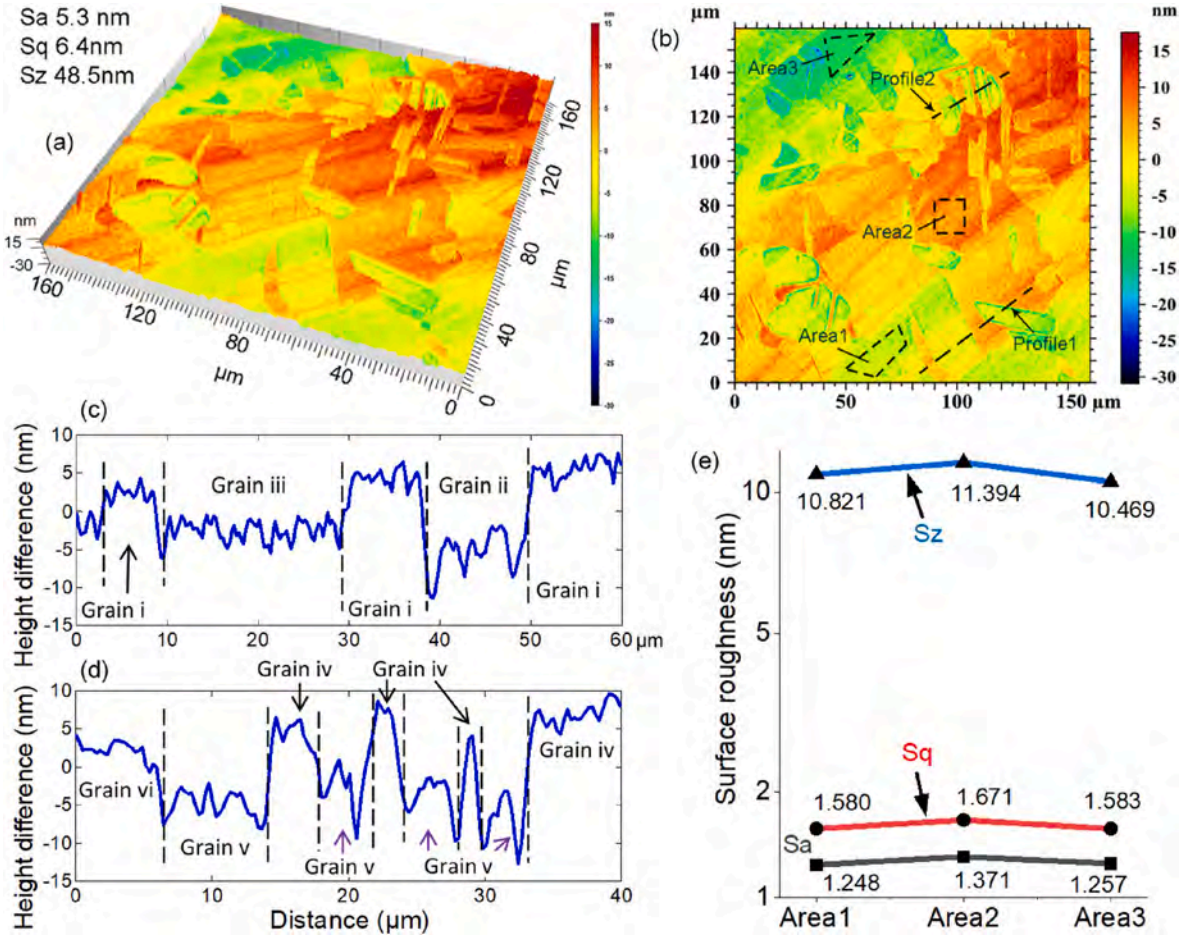

Fig. 18. (a) and (b) are isometric view and top view of 3D topography of the surface machined at a feed rate of 1 μm/rev; (c) and (d) are 2D surface profile along Line 1 and 2 marked in (b), respectively; (e) surface roughness of Area1 to 3 marked in (b).

boundaries of large grains rather than those of small grains due to excessive stress concentration on a unit per unit volume of grain boundary in the turning of monophasic polycrystalline metal [11]. Dislodgment will occur when the bonding strength at the grain boundary is low in the turning of sintered multiphase polycrystalline material [10]. However, in terms of ultraprecision turning of coarse-grained *p*-ZnSe, the undeformed chip thickness is far less than the grain size and the material is seen to possess low levels of hardness and fracture toughness. Consequently, the effect of stress on the grain boundary of *p*-ZnSe should be much smaller than that of the aforementioned polycrystalline materials. The brittle fracture inside the grains would, therefore, occur before the nucleation of cracks at the boundary. Hence, neither crack initiation at the grain boundary nor grain dislodgement would occur. This is likewise confirmed by the surface topography shown in Fig. 5, where homomorphic surface defects are limited inside specific grains and no cracks are generated at the grain boundary. Therefore, in the ultraprecision turning of coarse-grained *p*-ZnSe, the crystallographic effect plays a major factor in material removal, whereas that of grain size effect is not that significant. Consequently, the mechanism for machining can be simplified by considering individual grains

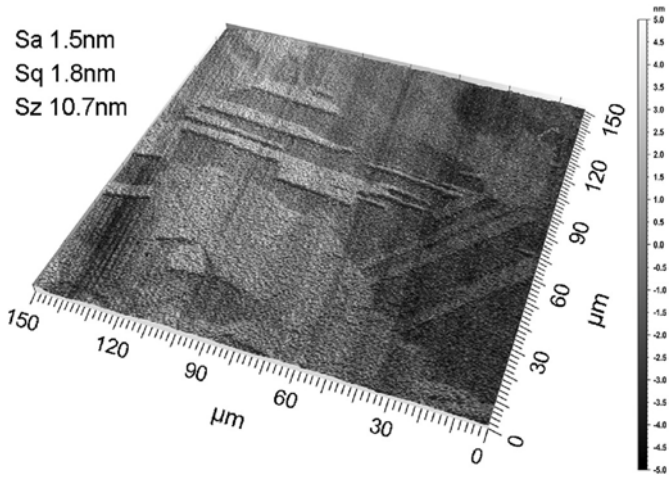

Fig. 19. 3D topography of a surface machined at a feed rate of 0.5 μm/rev.

with certain crystal orientations. By avoiding micron-craters and submicron-pits, a smooth machined surface can be realised without detectable defects.

Based on the foregoing analysis, to obtain a smooth surface without any defects, a cutting tool with a rake angle of 0° and a small relief angle is preferable. Moreover, the undeformed chip thickness should be sufficiently low so that all grains with various crystal orientations can be removed in a ductile mode.

4. Results of large nose radius (*R*10) tool

4.1. Surface roughness

Fig. 17(a) and (b) are SEM images randomly captured on a machined surface using the *R*10 tool, which presented no surface defects. Thereafter, a 3D topography of the machined surface was measured in a field of 160 × 160 μm^2 using a white light interferometer, as shown in Fig. 18 (a) and (b). The standard roughness parameters of the measured surface were defined by mean roughness (Sa), root mean square of roughness (Sq), and the maximum height of the profile (Sz). The Sa, Sq, and Sz of the surface were found to be 5.3 nm, 6.4 nm, and 48.5 nm, respectively. Fig. 18(c) and (d) give the extracted 2D surface profiles along Lines 1 and 2, marked in Fig. 18(b). In both profiles, grain boundary steps can be identified clearly. In Fig. 18(c), the height difference between grains i and ii is approximately 14 nm while that between grains i and iii is about 9 nm. In Fig. 18(d), the height difference between grains iv and v is about 18 nm while that between grains iv and vi is approximately 6 nm. Fig. 18(e) compares the surface roughness of three different grains that are marked in Fig. 18(b). The result shows that the surface roughness within each grain is similar but is much lower than the roughness of the whole measured surface. These indicate that the surface roughness is dominated by the grain boundary steps. In the ultraprecision cutting of polycrystalline germanium, the boundary step height was found to have decreased as the undeformed chip thickness decreased [20]. Therefore, to reduce the surface roughness of *p*-ZnSe, a smaller feed rate of 0.5 μm/rev was applied in this experiment. The 3D topography of the machined surface is shown in Fig. 19. The standard roughness parameters (i.e. Sa, Sq and Sz) were reduced to 1.5 nm, 1.8 nm, and 10.7 nm, respectively. It can also be seen from Fig. 19 that although the size of the grains with the same crystallographic orientation is different, the

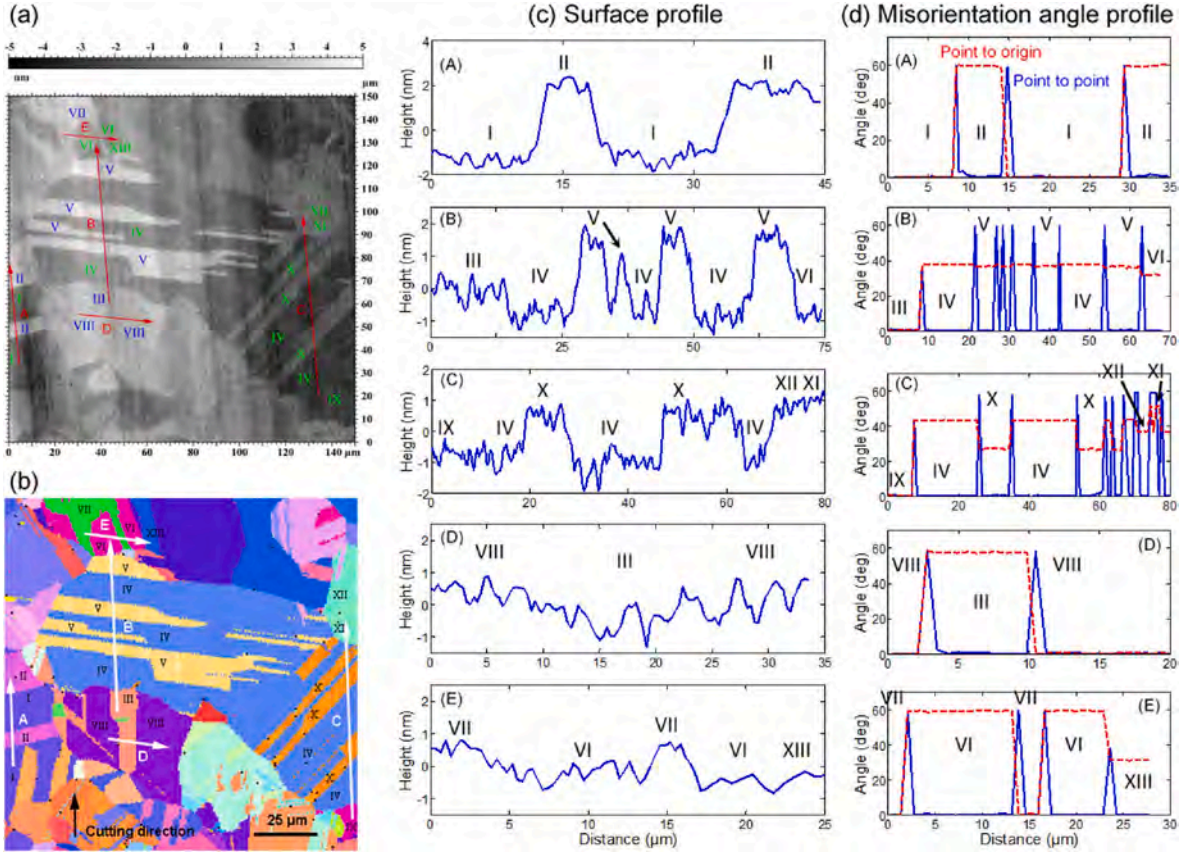

Fig. 20. (a) Top view of 3D topography of the surface shown in Fig. 18; (b) IPF map of the same surface shown in (a); (c) 2D surface profile along Lines A to E marked in (a); (d) misorientation angle profile along Lines A - E marked in (b).

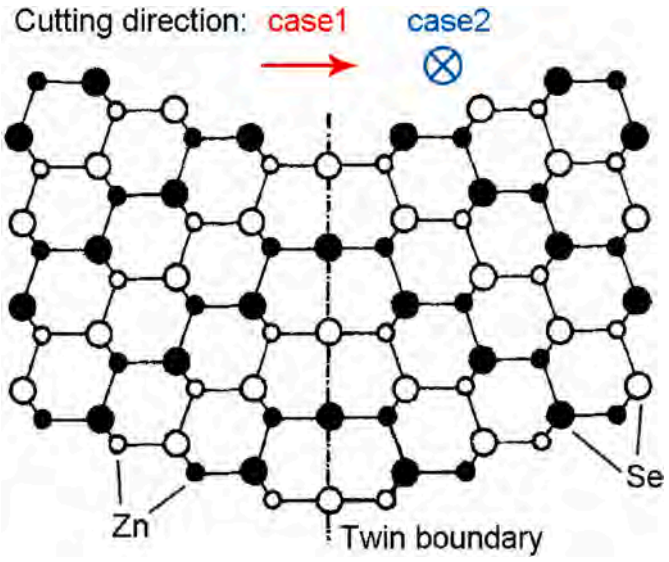

Fig. 21. Illustration of the relative position of cutting direction to a typical ZnSe twining (Zn and Se atoms are denoted by small and large circles, respectively) [58].

topography of these grains is the same. This is inconsistent with the Hall-Petch relationship (i.e. the yield stress will increase as the grain size decreases) [54]. This is because, in this study, the machining scale (undeformed chip thickness) is nanometric and far less than the grain size, which is in micron-scale or larger. Therefore, the surface roughness is mainly affected by crystal orientation.

4.2. Grain boundary step

Although the surface roughness decreases as the undeformed chip thickness decreases, the grain boundary step remains visible and dominates the surface roughness, as seen in Fig. 19. To further explore the formation mechanism of grain boundary step, EBSD analysis was conducted in combination with surface topography measurement. The top view of 3D surface topography is illustrated in Fig. 20(a) and the IPF map of the same area is illustrated in Fig. 20(b). The extracted 2D surface profiles along Lines A to E marked in the surface topography are presented in Fig. 20(c). The misorientation angle profiles along Lines A to E marked in the IPF map are shown in Fig. 20(d), as represented by the point-to-origin and point-to-point curves.

As seen in Fig. 20(c), on the one hand, the height difference between grains I and II in profile A, the height difference between grains IV and V in profile B, and the height difference between grains IV and X in profile C are obvious. On the other hand, the corresponding misorientation angle profiles (Fig. 20(d)) show that the misorientation angles between the two grains are at 60°, indicating that these boundaries are twin boundaries around <111> [55,56]. In addition, it can be noted that, in surface profile B, there is a small height difference between grains III and IV. The corresponding misorientation angle is 39°, indicating that the boundary is a twin boundary around <110> [55,57]. In misorientation angle profile C, there is a high-angle grain boundary of 43.6° between grains IX and IV, which is greater than 39°, however, the height difference between the two grains is unobvious. As such, the grain boundary step is easily formed at the twin boundary and a higher twin boundary misorientation angle leads to a higher grain boundary step. Besides, it can be noted that the boundary between grains VIII and III and that between grains VII and VI are also twin boundaries as indicated by misorientation angle profiles D and E. However, the corresponding grain boundary steps shown in surface profiles D and E are very small. This may be because the cutting direction is parallel to the twin boundary. Therefore, it can be deduced that the grain boundary step tends to form at the place where the cutting tool path crosses the twin boundary with a large angle.

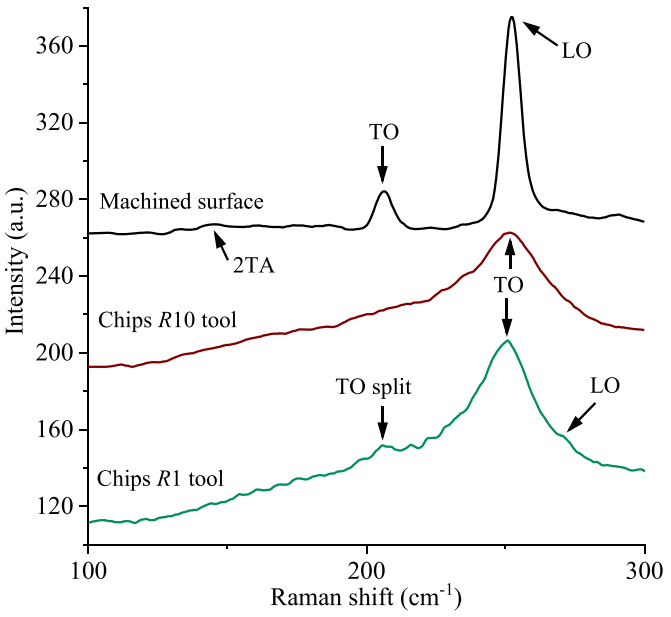

Fig. 22. Raman spectra of machined surface and the cutting chips by using *R*10 tool at $f = 1$ μm/rev.

A model of ZnSe twining has been established by Shiojiri et al. [58], as shown in Fig. 21. If the cutting direction is perpendicular to the twin boundary (Fig. 21, case 1), the twin-pair will exhibit different mechanical properties due to the different relative positions of cutting direction with crystal orientation, causing the difference in dislocation density in the twin-pair. Moreover, the twin boundaries are effective in stopping dislocations and preventing them from travelling into the adjoining-twin, as proven through a high-resolution TEM observation [59,60]. Additionally, the plastic deformation of the twin is highly dependent on dislocation [61]. This could lead to different levels of thickness of material removal that is plastically deformed in the twin-pair, causing the grain boundary step formation. It is also supported by the simulation result that the levels of chip thickness formed in two grains are different, as reported by Zhang et al. [12]. However, if the cutting direction is parallel to the twin boundary (Fig. 21, case 2) the twin-pair will exhibit the same mechanical properties and, consequently, no grain boundary step will be formed.

4.3. Metallization of cutting chips

Raman spectra of the machined surface and cutting chips obtained using a *R*10 tool are shown in Fig. 22. The Raman spectrum of cutting chips obtained using a *R*1 tool was likewise plotted for comparison. In the spectrum of cutting chips (*R*10 tool), the LO phonon peak disappeared, indicating that the cutting pressure is higher than 12.5 GPa and that ZnSe has transformed to a metal phase [38]. It is the metallization of cutting chips that helps the removal of the material from a completely ductile mode. On the other hand, the features of the spectrum of the machined surface using the *R*10 tool are similar to that with regard to the *R*1 tool (Fig. 12), however, the peak height of TO and LO phonon mode was found to be lower. This indicates once more that the phase transformation in the machined surface can be reversed to some extent after the tool passes. It should be noted that the 2 TA phonon peak on the machined surface of the *R*10 tool is very weak compared to that of the *R*1 tool. This may be due to fact that the phase stability of the lattice structure was broken at the high pressure [38] induced by the *R*10 tool, thereby preventing the recovery of the lattice crystalline phase after the tool passed. As a result, the reverse phase transformation was found to

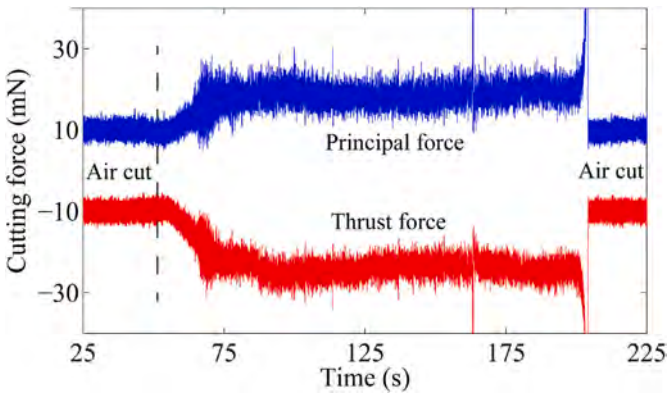

Fig. 23. The principal and thrust forces acting on the $R10$ tool measured at $f = 1$ μm/rev.

be incomplete for the $R10$ tool. Thus, it can be inferred that the thickness of phase transformation layer has been increased by the large radius tool.

The principal and thrust forces measured using the $R10$ tool are 8.33 mN and 14.25 mN, respectively, as shown in Fig. 23. The thrust force is larger than the principal force, which is similar to the result obtained using the $R1$ tool (Fig. 13, $f = 1$ μm/rev, $\alpha = 0°$). However, both the principal and thrust forces using the $R10$ tool are lower than those of the $R1$ tool. To figure out why chip metallization was observed for the $R10$ tool but not for the $R1$ tool, the cutting pressure, P, was estimated based on a simplified tool-workpiece contact model (Fig. A1). The value of P was calculated from the resulting cutting force, F, which is synthesised from the measured principal and thrust forces, as well as the contact area, A, between the workpiece and cutting tool. The detailed calculation procedures of the cutting pressure are given in the appendix of this paper. The calculated results show that the cutting pressures for the $R10$ tool and the $R1$ tool are 18.3 MPa and 5.6 MPa, respectively. These results are consistent with the pressure level reflected by their respective Raman spectra of cutting chips.

4.4. Tool wear

Fig. 24(a) and (b) show the SEM images of the cutting edges of an unused single-crystal diamond tool and the same tool after cutting for a distance of 5.5 km, respectively. In Fig. 24(a), the cutting edge is extremely sharp while the rake and flank faces are exceptionally smooth. However, after cutting, two kinds of wear patterns were identified, as shown in Fig. 24(b). One of the patterns pertains to the parallel grooves on the tool rake face possibly caused by the abrasive effect of chip flow. The other refers to a flank wear land which is smooth and uniform along the cutting edge, indicating that the friction between the tool and finished surface was steady during the cutting process. No edge chipping was observed due to the low level of hardness of ZnSe. However, since ZnSe is very brittle, an extremely low undeformed chip thickness should be set to achieve high surface integrity. To realise a low undeformed chip thickness, an extremely low feed rate is necessary for a small nose radius tool ($R1$), which leads to a very long distance of cutting for a large workpiece area. However, for a large nose radius tool ($R10$), the cutting distance for the same workpiece area is considerably smaller than that in relation to the $R1$ tool (i.e. cutting distance of $R10$ tool is only about one-third of the distance of the $R1$ tool to machine the same workpiece area). Consequently, the use of a large nose radius tool enables ductile mode cutting even with a large tool feed rate, which can reduce tool wear and machining time, and consequently, contribute to the productivity of IR optical components.

5. Conclusions

Ultraprecision diamond turning of polycrystalline ZnSe was conducted and the mechanisms for surface defect formation, phase transformation, chip formation, and grain boundary step formation were investigated. The major conclusions are summarised as follows:

(1) Unlike the machining of polycrystalline hard brittle ceramics and polycrystalline metals, no trans grain cracks nor grain dislodgements manifested in ultraprecision diamond turning of coarse-grained p-ZnSe. The surface defects arose within certain grains.
(2) Two kinds of surface defects were observed. One pertains to micron-craters formed on the grain whose cleavage plane is perpendicular to the cutting plane and cutting direction. The other refers to submicron-pits formed on the grain whose cleavage plane is perpendicular to the cutting plane.
(3) The micron-craters are caused by the cleavage fracture of the material at a large feed rate due to the plowing effects. The submicron-pits are caused by tearing and peeling of the material after the tool passes due to the elastic recovery at a negative rake angle.
(4) A large nose radius tool with a rake angle of 0° was effective in machining polycrystalline ZnSe. A smooth surface of 1.5 nm Sa without detectable defect was realised.

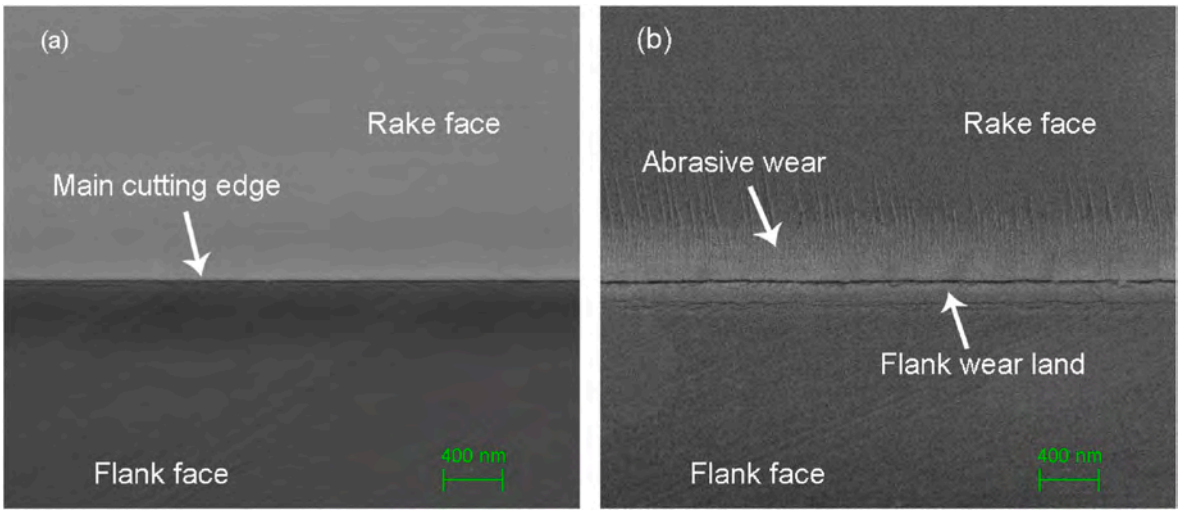

Fig. 24. SEM images of cutting edges of (a) an unused tool and (b) the same tool after cutting for 5.5 km.

(5) The final surface roughness is dominated by grain boundary steps. The grain boundary step tends to form at the place where the cutting tool path crosses the twin boundary with a large angle.
(6) Cutting chips undergo a zincblende to cinnabar phase transformation which is enhanced by the strong shear stress in the shear zone. The metallization of cutting chips occurs because of an extremely low undeformed chip thickness (~20 nm).
(7) When using a small radius tool, no residual phase change is detected from the machined surface. A reversed phase transformation from cinnabar to zincblende may occur after the tool passes.
(8) The dominant tool wear patterns are rubbing wear at the flank face and abrasive wear on the rake face with no edge chipping.

Declaration of competing interest

The authors declare that they have no known competing financial interests or personal relationships that could have appeared to influence the work reported in this paper.

CRediT authorship contribution statement

Weihai Huang: Data curation, Investigation, Writing - original draft. **Jiwang Yan:** Conceptualization, Methodology, Supervision, Writing - review & editing.

Acknowledgements

This work has been partially supported by Keio University Doctorate Student Grant-in-Aid Program. Thanks are extended to Mrs. Sachiko Kamiyama of Central Testing Center, Keio University for her assistance of SEM and EBSD observations.

Appendix A. Calculation of cutting pressure

This appendix elaborates the calculation procedure of cutting pressure, P, the results of which having been used in Section 4.3.

Cutting pressure P can be expressed as:

$$P = \frac{F}{A}. \tag{A.1}$$

$$F = {F_p}^2 + {F_t}^2. \tag{A.2}$$

where F is the resultant cutting force, which is derived from the experimentally measured principal force, F_p, and thrust force, F_t. A pertains to the contact area between the tool edge and workpiece.

For a visualisation of contact area A, firstly, a model of undeformed chip cross-section was schematised, as shown in Fig. A.1. The undeformed chip thickness, h, varies with angular position, δ, along the tool nose, which gradually increases from zero to the maximum value, h_{max}, and then decreases to zero. Thus, the h and h_{max} can be expressed as follows:

$$h = \begin{cases} R - \sqrt{R^2 + f^2 - 2Rf\cos\left(\frac{\pi}{2} - \delta\right)} & \delta_{\min} \le \delta \le \delta_{\max} \\ R - \dfrac{R-d}{\cos\delta} & \delta'_{\min} \le \delta \le \delta'_{\max} \end{cases} \tag{A.3}$$

$$h_{\max} = R - \sqrt{R^2 + f^2 - 2f\sqrt{2Rd - d^2}} \tag{A.4}$$

where $\delta_{\min} = \arcsin\left(\frac{f}{2R}\right)$, $\delta_{\max} = \arccos\left(\frac{R-d}{R}\right)$, $\delta_{\min} = \arccos\left(\frac{R-d}{R-h_{\max}}\right)$, $\delta'_{\max} = \arccos\left(\frac{R-d}{R}\right)$.

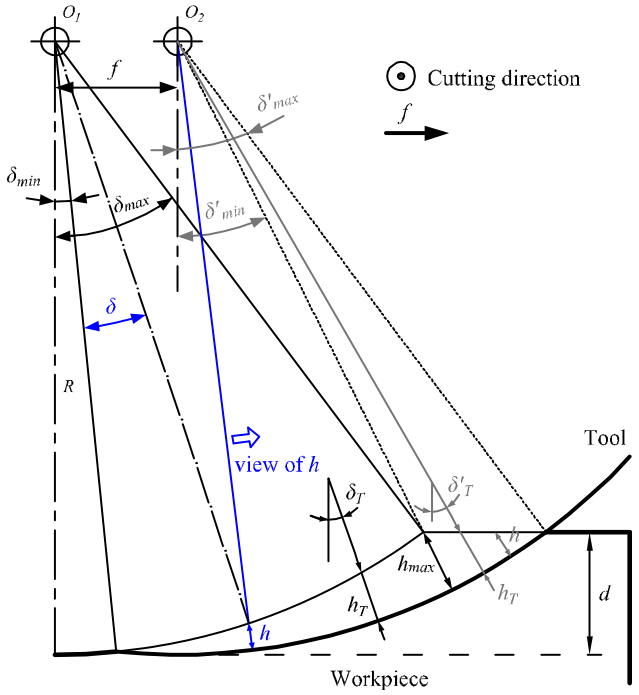

Fig. A.1. Schematic model of the undeformed chip cross-section.

For each h (angular position δ) shown in Fig. A.1, from the view of parallel to cutting direction, the schematic model of the contact length between the cutting tool and the workpiece can be plotted, as shown in Fig. A.2. In this simplified model, the contact between the cutting chips and tool rake face, as well as that between the machined surface and tool flank face were neglected. As exhibited in Fig. A.2, T is the point where the rake face is tangent to the tool edge radius, r. If the h is smaller than the height of point T (h_T), only the tool edge contacts the workpiece. On the other hand, if the h is larger than the h_T, both tool edge and rake face contact the workpiece. Therefore, the contact length, l, can be computed as follows:

$$l = \begin{cases} r \cdot \operatorname{arccot}\left(\dfrac{r-h}{r}\right) & h < h_T \\ r \cdot \left(\dfrac{\pi}{2} - \alpha\right) + \dfrac{h - h_T}{\cot \alpha} & h \geq h_T \end{cases} \tag{A.5}$$

$$h_T = r - r \cdot \sin \alpha \tag{A.6}$$

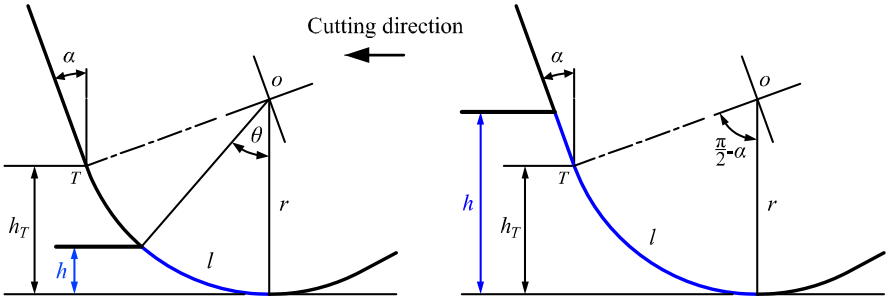

Fig. A.2. Schematic model of the contact geometry between cutting tool and workpiece (view from the direction parallel to cutting direction).

According to Eq. (A.4), the h_{max} using the $R10$ and $R1$ tools are 20 nm and 63 nm, respectively. The h_T at the tool edge radius of 50 nm and rake angle of 0° is 50 nm, as shown by Eq. (A.6). Thus, for the $R10$ tool, at any angular position, δ, only the tool edge comes in contact with the workpiece. For the $R1$ tool, at the angular positions $\delta_T < \delta < \delta_{max}$ and $\delta'_{min} < \delta < \delta'_T$, the tool rake face will also make contact with the workpiece. The δ_T and δ'_T can be solved by substituting Eq. (A.6) into Eq. (A.3).

$$\delta_T = \arcsin\left(\frac{R^2 + f^2 - [R - r(1 - \sin \alpha)]^2}{2Rf}\right) \tag{A.7}$$

$$\delta'_T = \arccos\left(\frac{R - d}{R - r + r \sin \alpha}\right) \tag{A.8}$$

After which, substituting Eq. (A.3) into Eq. (A.5) can lead to obtaining the relations between contact length, l, and angular position, δ:

for the $R10$ tool,

$$l_{1,\ 2} = \begin{cases} r\cdot\operatorname{arccot}\left(\dfrac{r-h_1}{r}\right) & \delta_{\min} \le \delta \le \delta_{\max} \\ r\cdot\operatorname{arccot}\left(\dfrac{r-h_2}{r}\right) & \delta'_{\min} \le \delta \le \delta'_{\max} \end{cases} \tag{A.9}$$

for the $R1$ tool,

$$l_{1,\ 2,\ 3,\ 4} = \begin{cases} r\cdot\operatorname{arccot}\left(\dfrac{r-h_1}{r}\right) & \delta_{\min} \le \delta \le \delta_T \\ r\cdot\left(\dfrac{\pi}{2}-\alpha\right)+\dfrac{h_1-h_T}{\cot\alpha} & \delta_T \le \delta \le \delta_{\max} \\ r\cdot\left(\dfrac{\pi}{2}-\alpha\right)+\dfrac{h_2-h_T}{\cot\alpha} & \delta'_{\min} \le \delta' \le \delta'_T \\ r\cdot\operatorname{arccot}\left(\dfrac{r-h_2}{r}\right) & \delta'_T \le \delta' \le \delta'_{\max} \end{cases} \tag{A.10}$$

where $h_1 = R - \sqrt{R^2+f^2-2Rf\cos\left(\frac{\pi}{2}-\delta\right)}$ and $h_2 = R - \frac{R-d}{\cos\delta}$.

Therefore, the contact area, A, can be expressed as follows: for the $R10$ tool,

$$A = \int_{\delta_{\min}}^{\delta_{\max}} l_1 \mathrm{d}\delta + \int_{\delta'_{\min}}^{\delta'_{\max}} l_2 \mathrm{d}\delta' \tag{A.11}$$

for the $R1$ tool,

$$A = \int_{\delta_{\min}}^{\delta_T} l_1 \mathrm{d}\delta + \int_{\delta_T}^{\delta_{\max}} l_2 \mathrm{d}\delta + \int_{\delta'_{\min}}^{\delta'_T} l_3 \mathrm{d}\delta' + \int_{\delta'_T}^{\delta'_{\max}} l_4 \mathrm{d}\delta' \tag{A.12}$$

Using the numerical method, the contact area, A, can be easily calculated. The contact areas, A, at $R10$ and $R1$ tool are 9.02×10^{-10} m^2 and 3.89×10^{-9} m^2, respectively. The calculated cutting pressures using the $R10$ tool and the $R1$ tool are 18.3 MPa and 5.6 MPa, respectively.

References

[1] Q. Zhang, H. Li, Y. Ma, T. Zhai, ZnSe nanostructures: synthesis, properties and applications, Prog. Mater. Sci. 83 (2016) 472–535.
[2] E.M. Gavrushchuk, Polycrystalline zinc selenide for IR optical applications, Inorg. Mater. 39 (2003) 883–899.
[3] Y. Jia, F. Chen, Optical channel waveguides in ZnSe single crystal produced by proton implantation, Opt. Mater. Express 2 (2012) 455–460.
[4] E.V. Abakumova, M.N. Achasov, A.A. Krasnov, N.Y. Muchnoi, E.E. Pyata, The system for delivery of IR laser radiaton into high vacuum, J. Instrum. 10 (2015) T9001.
[5] S.E. Grillo, M. Ducarroir, M. Nadal, E. Tourni, J. Faurie, Nanoindentation of Si, GaP, GaAs and ZnSe single crystals, J. Phys. Appl. Phys. 36 (2002) L5–L9.
[6] S. Freiman, The fracture of glass: past, present, and future, Int. J. Appl. Glass Sci. 3 (2012) 89–106.
[7] E.Y. Vilkova, O.V. Timofeev, Etching and chemical mechanical polishing of ZnSe using inorganic acids, Inorg. Mater. 48 (2012) 451–455.
[8] O.V. Timofeev, E.Y. Vilkova, Effect of etching and chemomechanical polishing on the surface quality of polycrystalline ZnSe, Inorg. Mater. 46 (2010) 259–263.
[9] W.J. Zong, Z.M. Cao, C.L. He, C.X. Xue, Theoretical modelling and FE simulation on the oblique diamond turning of ZnS crystal, Int. J. Mach. Tool Manufact. 100 (2016) 55–71.
[10] J. Yan, Z. Zhang, T. Kuriyagawa, Mechanism for material removal in diamond turning of reaction-bonded silicon carbide, Int. J. Mach. Tool Manufact. 49 (2009) 366–374.
[11] Z. Zhao, S. To, J. Wang, Effects of grains and twins on deformation of commercial pure titanium in ultraprecision diamond turning, J. Mater. Process. Technol. 271 (2019) 10–22.
[12] Z. Wang, J. Zhang, Z. Xu, J. Zhang, H.U. Hassan, G. Li, H. Zhang, A. Hartmaier, F. Fang, Y. Yan, T. Sun, Crystal plasticity finite element modeling and simulation of diamond cutting of polycrystalline copper, J. Manuf. Process. 38 (2019) 187–195.
[13] F.Z. Fang, V.C. Venkatesh, G.X. Zhang, Diamond turning of soft semiconductors to obtain nanometric mirror surfaces, Int. J. Adv. Manuf. Technol. 19 (2002) 637–641.
[14] S.A. Shojaee, T.A. Harriman, Y. Qi, D.A. Lucca, B.S. Dutterer, M.A. Davies, T. J. Suleski, Spatial variations in stress and crystal quality in diamond turned ZnSe surfaces measured by Raman spectroscopy, Manufacturing Letters 2 (2014) 35–39.
[15] W. Li, K. Yang, P. Wang, G. Zhang, D. Liu, Experimental investigation of the ultra-precision turning capability of PVD ZnSe. Proc, 8th International Symposium on Advanced Optical Manufacturing and Testing Technology: Advanced Optical Manufacturing Technologies, SPIE Suzhou, China, 2016.
[16] H. Xiao, R. Liang, O. Spires, H. Wang, H. Wu, Y. Zhang, Evaluation of surface and subsurface damages for diamond turning of ZnSe crystal, Optic Express 27 (2019) 28364–28382.
[17] E.M. Gavrishchuk, É.V. Yashina, Zinc sulfide and zinc selenide optical elements for IR engineering, J. Opt. Technol. 71 (2004) 822–827.
[18] J. Yu, G. Wang, Y. Rong, Experimental Study on the surface integrity and chip formation in the micro cutting process, Procedia Manufacturing 1 (2015) 655–662.
[19] E. Brinksmeier, W. Preuss, O. Riemer, R. Rentsch, Cutting forces, tool wear and surface finish in high speed diamond machining, Precis. Eng. 49 (2017) 293–304.
[20] J. Yan, Y. Takahashi, J.R. Tamaki, Ichi, A. Kubo, T. Kuriyagawa, Y. Sato, Ultraprecision machining characteristics of poly-crystalline germanium, JSME International Journal Series C Mechanical Systems, Machine Elements and Manufacturing 49 (2006) 63–69.
[21] S. Venkatachalam, O. Fergani, X. Li, J. Guo Yang, K. Chiang, S.Y. Liang, Microstructure effects on cutting forces and flow stress in ultra-precision machining of polycrystalline brittle materials, J. Manuf. Sci. Eng. 137 (2015).
[22] Z. Wang, J. Zhang, J. Zhang, G. Li, H. Zhang, H. Ul Hassan, A. Hartmaier, Y. Yan, T. Sun, Towards an understanding of grain boundary step in diamond cutting of polycrystalline copper, J. Mater. Process. Technol. 276 (2020) 116400.
[23] Z. Wang, T. Sun, H. Zhang, G. Li, Z. Li, J. Zhang, Y. Yan, A. Hartmaier, The interaction between grain boundary and tool geometry in nanocutting of a bi-crystal copper, International Journal of Extreme Manufacturing 1 (2019) 45001.
[24] D. Liu, G. Wang, J. Yu, Y.K. Rong, Molecular dynamics simulation on formation mechanism of grain boundary steps in micro-cutting of polycrystalline copper, Comput. Mater. Sci. 126 (2017) 418–425.
[25] N.A. Sakharova, J.V. Fernandes, J.M. Antunes, M.C. Oliveira, Comparison between Berkovich, Vickers and conical indentation tests: a three-dimensional numerical simulation study, Int. J. Solid Struct. 46 (2009) 1095–1104.
[26] T. Zhang, Y. Feng, R. Yang, P. Jiang, A method to determine fracture toughness using cube-corner indentation, Scripta Mater. 62 (2010) 199–201.
[27] J.V. Chang, Trends in Condensed Matter Physics Research, Nova Science Publishers, New York, 2006.
[28] T. Ohta, J. Yan, S. Yajima, Y. Takahashi, N. Horikawa, T. Kuriyagawa, High-efficiency machining of single-crystal germanium using large-radius diamond tools, Int. J. Surf. Sci. Eng. 1 (2007).
[29] S. Son, H. Lim, J. Ahn, The effect of vibration cutting on minimum cutting thickness, Int. J. Mach. Tool Manufact. 46 (2006) 2066–2072.

[30] Y. Sun, Z. Sun, S. Gao, H. Cheng, Q. Liu, J. Piao, T. Yao, C. Wu, S. Hu, S. Wei, Y. Xie, Fabrication of flexible and freestanding zinc chalcogenide single layers, Nat. Commun. 3 (2012) 1057.
[31] O.A. Fedorenko, Y.A. Zagoruiko, N.O. Kovalenko, Mechanical properties of ZnSe : Cr2+ single crystals, Phys. Solid State 54 (2012) 2253–2255.
[32] M.Q. Jiang, L.H. Dai, Formation mechanism of lamellar chips during machining of bulk metallic glass, Acta Mater. 57 (2009) 2730–2738.
[33] K. Liu, X.P. Li, M. Rahman, K.S. Neo, X.D. Liu, A study of the effect of tool cutting edge radius on ductile cutting of silicon wafers, Int. J. Adv. Manuf. Technol. 32 (2007) 631–637.
[34] S. Ning, G. Feng, H. Zhang, W. Zhang, S. Dai, S. Zhou, Fabrication, structure and optical application of Fe2+:ZnSe nanocrystalline film, Opt. Mater. 89 (2019) 473–479.
[35] L.D. Yao, F.F. Wang, X. Shen, S.J. You, L.X. Yang, S. Jiang, Y.C. Li, K. Zhu, Y.L. Liu, A.L. Pan, B.S. Zou, J. Liu, C.Q. Jin, R.C. Yu, Structural stability and Raman scattering of ZnSe nanoribbons under high pressure, J. Alloys Compd. 480 (2009) 798–801.
[36] M. Mukaida, J. Yan, Ductile machining of single-crystal silicon for microlens arrays by ultraprecision diamond turning using a slow tool servo, Int. J. Mach. Tool Manufact. 115 (2017) 2–14.
[37] J. Yan, Laser micro-Raman spectroscopy of single-point diamond machined silicon substrates, J. Appl. Phys. 95 (2004) 2094–2101.
[38] C. Pu, L. Dai, H. Li, H. Hu, K. Liu, L. Yang, M. Hong, Pressure-induced phase transitions of ZnSe under different pressure environments, AIP Adv. 9 (2019) 25004.
[39] J. Yan, T. Asami, T. Kuriyagawa, Nondestructive measurement of machining-induced amorphous layers in single-crystal silicon by laser micro-Raman spectroscopy, Precis. Eng. 32 (2008) 186–195.
[40] Z. Zhao, S. To, Z. Zhu, T. Yin, A theoretical and experimental investigation of cutting forces and spring back behaviour of Ti6Al4V alloy in ultraprecision machining of microgrooves, Int. J. Mech. Sci. 169 (2020) 105315.
[41] M. Günay, E. Aslan, İ. Korkut, U. Şeker, Investigation of the effect of rake angle on main cutting force, Int. J. Mach. Tool Manufact. 44 (2004) 953–959.
[42] J. Yan, T. Asami, H. Harada, T. Kuriyagawa, Fundamental investigation of subsurface damage in single crystalline silicon caused by diamond machining, Precis. Eng. 33 (2009) 378–386.
[43] M. Wan, D. Wen, Y. Ma, W. Zhang, On material separation and cutting force prediction in micro milling through involving the effect of dead metal zone, Int. J. Mach. Tool Manufact. 146 (2019) 103452.
[44] F.Z. Fang, H. Wu, W. Zhou, X.T. Hu, A study on mechanism of nano-cutting single crystal silicon, J. Mater. Process. Technol. 184 (2007) 407–410.
[45] W. Huang, D. Yu, M. Zhang, Q. Cao, J. Yao, Predictive cutting force model for ductile-regime machining of brittle materials, Int. J. Adv. Manuf. Technol. 98 (2018) 781–790.
[46] X. Liu, R.E. DeVor, S.G. Kapoor, An analytical model for the prediction of minimum chip thickness in micromachining, J. Manuf. Sci. Eng. 128 (2005) 474–481.
[47] S.M. Son, H.S. Lim, J.H. Ahn, Effects of the friction coefficient on the minimum cutting thickness in micro cutting, Int. J. Mach. Tool Manufact. 45 (2005) 529–535.
[48] W.S. Yip, S. To, Reduction of minimum cutting thickness of titanium alloys in micro cutting by a magnetic field assistance, IEEE Access, 2019, p. 1.
[49] X. Chen, J. Xu, H. Fang, R. Tian, Influence of cutting parameters on the ductile-brittle transition of single-crystal calcium fluoride during ultra-precision cutting, Int. J. Adv. Manuf. Technol. 89 (2017) 219–225.
[50] J. Yan, K. Syoji, T. Kuriyagawa, Ductile-brittle transition at large negative tool rake angles, J. Jpn. Soc. Precis. Eng. 66 (2000) 1130–1134.
[51] F.Z. Fang, H. Wu, Y.C. Liu, Modelling and experimental investigation on nanometric cutting of monocrystalline silicon, Int. J. Mach. Tool Manufact. 45 (2005) 1681–1686.
[52] J. Yan, K. Syoji, T. Kuriyagawa, H. Suzuki, Ductile regime turning at large tool feed, J. Mater. Process. Technol. 121 (2002) 363–372.
[53] A. Mir, X. Luo, J. Sun, The investigation of influence of tool wear on ductile to brittle transition in single point diamond turning of silicon, Wear 364–365 (2016) 233–243.
[54] J. Shi, Y. Wang, X. Yang, Nano-scale machining of polycrystalline coppers - effects of grain size and machining parameters, Nanoscale Research Letters 8 (2013) 500.
[55] R.H. Geiss, D.T. Read, Need for standardization of EBSD measurements for microstructural characterization of thin film structures, AIP Conference Proceedings 931 (2007) 168–172.
[56] J. Jung, J.I. Yoon, J.G. Kim, M.I. Latypov, J.Y. Kim, H.S. Kim, Continuum understanding of twin formation near grain boundaries of FCC metals with low stacking fault energy, npj Computational Materials 3 (2017) 21.
[57] K.W. Ingle, A.G. Crocker, On the structure of high-angle (110) CSL twist boundaries in f.c.c. metals, Philos. Mag. A 41 (1980) 713–721.
[58] M. Shiojiri, C. Kaito, S. Sekimoto, N. Nakamura, Polarity and inversion twins in ZnSe crystals observed by high-resolution electron microscopy, Philos. Mag. A 46 (1982) 495–505.
[59] M. Dao, L. Lu, Y.F. Shen, S. Suresh, Strength, strain-rate sensitivity and ductility of copper with nanoscale twins, Acta Mater. 54 (2006) 5421–5432.
[60] C.J. Shute, B.D. Myers, S. Xie, T.W. Barbee, A.M. Hodge, J.R. Weertman, Microstructural stability during cyclic loading of multilayer copper/copper samples with nanoscale twinning, Scripta Mater. 60 (2009) 1073–1077.
[61] J. Li, B. Liu, H. Luo, Q. Fang, Y. Liu, Y. Liu, A molecular dynamics investigation into plastic deformation mechanism of nanocrystalline copper for different nanoscratching rates, Comput. Mater. Sci. 118 (2016) 66–76.